2017

Single-particle cryo-EM of the ryanodine receptor from skeletal muscle: reconstitution into nanodiscs and the conformational effects of magnesium.

Alex H. Will
Virginia Commonwealth University

Single-particle cryo-EM of the ryanodine receptor from skeletal muscle: reconstitution into nanodiscs and the conformational effects of magnesium.

A thesis submitted in partial fulfillment of the requirements for the degree of Master of Science in Physiology and Biophysics at Virginia Commonwealth University.

by

Alex H. Will,
Bachelor of Science, University of Virginia 2014

Director: Montserrat Samsó, Ph. D.
Department of Physiology and Biophysics

Virginia Commonwealth University
Richmond, Virginia
August, 2017

Acknowledgment

I wish to thank my mother and father for their undying love and support while I was in undergraduate and graduate school. I want to thank my brother, Scott, for always believing in me. I thank my girlfriend, Christel, for her support and understanding throughout the past year. I would like to thank my lab mates, Sonali, Josh, Faouzi, Ashok, Kavita, and Younus for their continued advice and instruction and for making my time in the laboratory enjoyable. I want to thank Dr. Jose Miguel Eltit and Dr. John Bigbee for agreeing to serve on my committee and for their direction during this process. Last but certainly not least, I thank Dr. Montserrat Samsó for agreeing to allow me to join her laboratory and for the extraordinary amount of information she taught me.

Table of Contents

List of Tables

List of Figures

List of Abbreviations

Abstract

SINGLE-PARTICLE CRYO-EM OF THE RYANODINE RECEPTOR FROM SKELETAL MUSCLE: RECONSTITUTION INTO NANODISCS AND THE CONFORMATIONAL EFFECTS OF MAGNESIUM

Alex H. Will,
Bachelor of Science, University of Virginia 2014

A thesis submitted in partial fulfillment of the requirements for the degree of Master of Science in Physiology and Biophysics at Virginia Commonwealth University.

Virginia Commonwealth University
Richmond, Virginia
August, 2017

Director: Montserrat Samsó, Ph. D.
Department of Physiology and Biophysics

The RyR1 acts as an intracellular calcium channel that allows passage of Ca^{2+} from the sarcoplasmic reticulum to the cytoplasm; this increase in cytosolic Ca^{2+} is required for excitation-contraction coupling. Certain mutations in RyR1 have been directly linked to malignant hyperthermia (MH) and central core disease. In a series of studies, the role of Mg^{2+} has been explored as it pertains to MH, and it has been determined that dysregulation of Mg^{2+} can even lead to MH in patients without mutations. Consequently, the aim of the study was to insert the RyR1 into nanodiscs, small, circular lipid bilayers used to solubilize membrane proteins, and to use cryo-electron microscopy to assess the conformation of the RyR1 in the presence of Mg^{2+} and AMP-PCP. Particle reconstruction generated a 9.0 Å resolution map that

confirmed successful incorporation of the RyR1 into nanodiscs and allowed visualization of the RyR1 in a physiological closed state.

1. Introduction

1.1. Ryanodine Receptor

1.1.1. Role in Excitation-Contraction Coupling

Throughout muscle types and even in brain tissue, there exist three major forms of the ryanodine receptor; each are given the abbreviation RyR followed by numbers one through three. Ryanodine receptor 1 (RyR1) is expressed predominately in skeletal muscle, ryanodine receptor 2 (RyR2) in cardiomyocytes, and ryanodine receptor 3 (RyR3) in brain cells.[1,2] Of note, all three isoforms are expressed in the brain to some extent. Each of the ryanodine receptors assemble as tetramers and act as intracellular calcium channels that release Ca^{2+} ions from the sarcoplasmic or endoplasmic reticulum into the cytoplasmic space. Regarding the case of RyR1, the calcium release is modulated through direct physical connection to the $Ca_V1.1$, or the dihydropyridine receptor (DHPR); the DHPR responds to nervous stimulation and activates (opens) the RyR1 to allow Ca^{2+} to flow from the SR to the cytoplasm. This direct contact is at the triad junction, where the transverse (T) tubule meets the endoplasmic or sarcoplasmic reticulum (ER or SR, respectively) on both sides of the tubule.[3]

In the case of the RyR2, calcium-induced calcium release is the means of Ca^{2+} efflux from the SR since the RyR2 is not directly opposing the $Ca_V1.2$. The T tubule meets the sarcoplasmic reticulum at a dyad. There, a neuronal impulse allows Ca^{2+} into the cell, activating the RyR2. Of note, it is referred to as a dyad because the opposition to the T tubule is only on one side.[4]

The cytosolic Ca^{2+} is required for excitation-contraction coupling leading to muscle contraction. The increased level of cytosolic Ca^{2+} allows for binding to troponin C of the troponin complex. This results in a conformational change of troponin I and tropomyosin so that the myosin binding site of an actin filament is exposed. Myosin may then bind to its respective site on the actin filament, and contraction can proceed through cross-bridge cycling. The figure below summarizes the DHPR (L-type Ca^{2+} channel) interaction with the ryanodine receptor, the role of the ryanodine receptor in Ca^{2+} release, the role of Ca^{2+} in troponin binding, and the opposition of the T-tubule to the SR (Figure 1).[5]

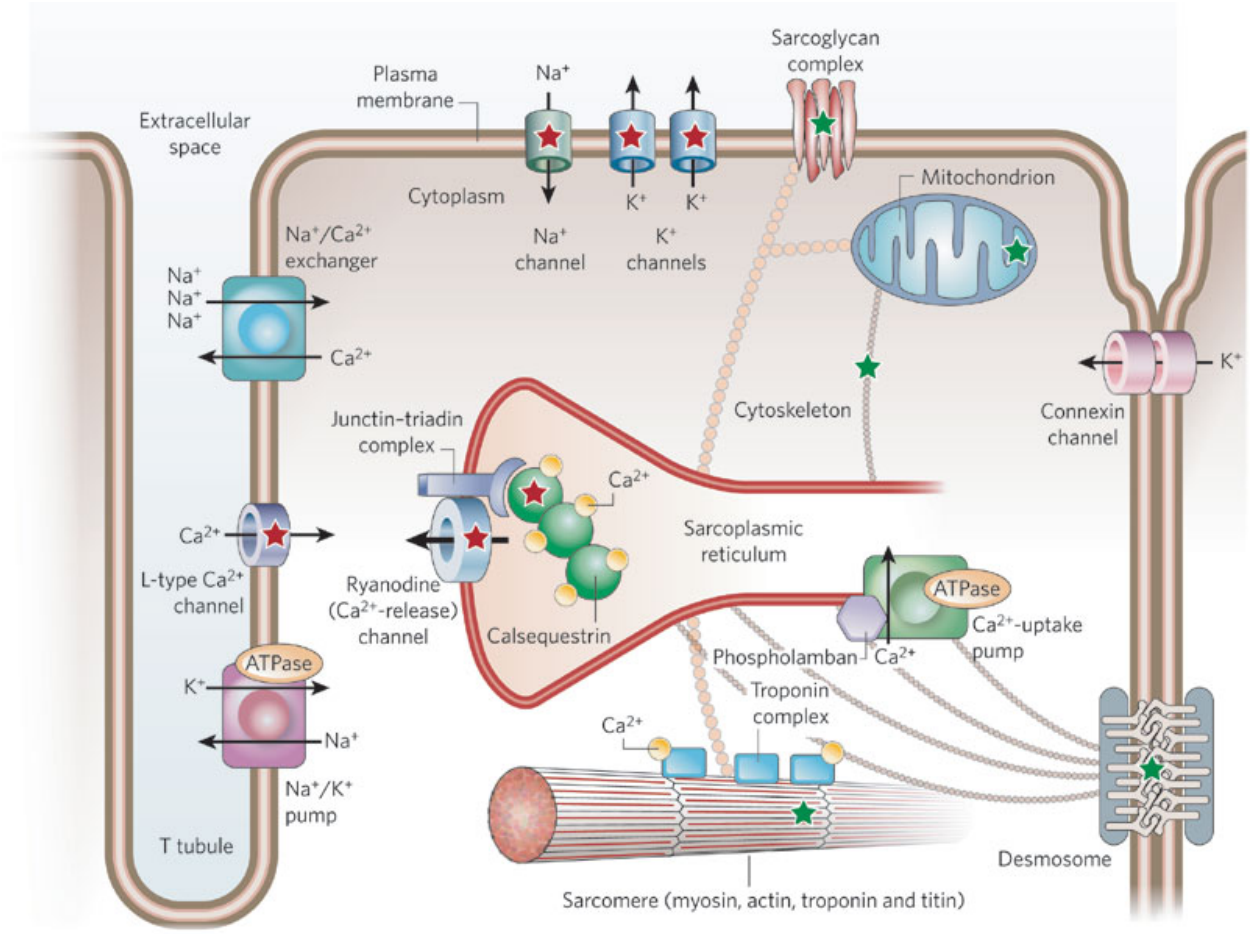

Figure 1. Diagram of RyR1 role in Ca^{2+} release and muscle contraction adapted from Bernstein et al. (2013)[5]

1.1.2. Mutations in the Ryanodine Receptor

Mutations in the type of isoform of the ryanodine receptor result in different pathologies due to their respective locations in different organs. A 2015 paper cites that over 500 mutations in the primary sequence of RyR1 and RyR2 have been shown to result in disease.[6] Of these, select mutations in the primary sequence of RyR1 can lead to central core disease (CCD) and also malignant hyperthermia (MH). A 2014 paper discusses 13 mutations that have been studied for their causal role in MH; these mutations typically cluster in the N-terminal and central domains, but there are instances of C-terminal domain mutations leading to MH.[7,8] There is no routine testing performed for mutations that lead to MH, so most patients do not know they are a carrier until in an MH crisis.

1.1.3. RyR1 Role in Malignant Hyperthermia and Central Core Disease

Malignant hyperthermia (MH) is an autosomal-dominant inherited disease that manifests as crises in susceptible individuals.[8] Crises occur in between 1:10,000 and 1:250,000 cases of anesthesia as a result of administration of volatile halogenated anesthetics in susceptible patients, and these crises may occur at any time between initial administration of the anesthetic and one hour after termination of the anesthetic dosing.[9,10] MH presents with a multitude of the following symptoms, which can lead to death if not treated immediately: pyrexia, hyperkalemia, hypercapnia, hypoxemia, cardiac arrhythmia, tachycardia, muscular rigidity, metabolic acidosis, and late-onset rhabdomyolysis.[8,11] The pathophysiological explanation involves structural changes to the ryanodine receptor 1 (RyR1) that lead to functional changes; specifically, the

RyR1 is left constitutionally activated (opened) resulting in the preliminary symptom of muscle rigidity.[12] Fortunately, most operating theaters in the developed world carry dantrolene, a medication that reverses the symptoms and effects of MH.[13]

Central core disease (CCD) can be both an autosomal-dominant and autosomal-recessive inherited disease that affects approximately 1 in 17,000 live births.[14,15] Patients with CCD are more prone to MH and vice versa.[16] Patients with dominantly inherited CCD typically present in infancy with hypotonia and in childhood with muscle stiffness and weakness on exertion as a result of developmental muscle delay.[17] Most patients are able to achieve independence while walking with the exception of the most severe cases in neonates.[18] Once again, the pathophysiological explanation involves structural changes to the RyR1 that lead to functional changes; one leading hypothesis is that CCD results from RyR1 adopting a "leaky" conformation that leads to disruption of muscle contraction.[19]

1.1.4. Structure and Domains of the RyR1

The cytoplasmic region of the RyR1 has a square face of dimensions 275 x 275 $Å^2$. With the inclusion of the transmembrane region, the receptor adopts more of a pyramidal shape with a height of 175 Å. The four subdomains of the receptor can be viewed as triangles forming the pyramidal quaternary structure. The N-terminal domain is located on the distal portion of the cytosolic face and is comprised of four domains, one per subunit. Each are divided into three subdomains of A, B, and C; A and B are predominately beta sheets, whereas C is entirely comprised of alpha-helices.[20]

Each subunit additionally consists of three SPRY domains; the SPRY1 domain is situated on the perimeter and serves for FKBP12 binding, the SPRY2 domain is thought to interact with the Cav1.1 subunits of the DHPR and is located behind the SPRY1 domain, and the SPRY3 domain is at the most distal cytosolic surface.[21,22,23] The function of the SPRY3 domain has not been biochemically studied, but with its location at the cytosolic face, its function can be speculated as plausible in the DHPR interaction.[24]

The handle domain is located at the base of the cytosolic face and creates portions of the binding sites for FKBP12 and calmodulin. This handle domain is connected to the SPRY2 domain of the neighboring subunit by the helical domains. These domains have a particular flexibility associated with them and have been implicated in giving the RyR1 its elasticity and ability to recoil to different conformations.

The P1 domain of the receptor is at the most distal portion of the clamp domains of the corners of the ryanodine receptor, and it originates from the SPRY domains.[24] The P2 domain contains phosphorylation site 2808 and 2814 and is suspected to vary immensely based on the phosphorylation state. As a consequence, the structure has not been resolved except for at a low resolution.

The central domains are located under the N-terminal domains and behind the handle domains. They are on the bottom of the cytoplasmic face and interact with the transmembrane region. In the central domain, two EF hands are present and thought to provide a portion of the Ca^{2+}-sensing ability of the RyR1.[25] A portion of the central domains comprises a 'U' shaped structure towards the center of the RyR1 called the U-motif. Lastly, the central domains ultimately give rise to the C-terminal domains, bulky domains at the end of the inner branches, the cytoplasmic protrusion of the S6 transmembrane helices.

The C-terminal domains comprise a portion of the cytoplasmic region of the receptor that alters in conformation as the ion gate closes in the closed conformation of the receptor.[26] The C-terminal domains additionally contain a stabilizing zinc-finger surrounded by the U-motif of the central domains.

The transmembrane region of the ryanodine receptor contains four transmembrane helices (S1-S4) oriented in a helical bundle similar to that of the K^+ channel that share similarities to voltage-sensing domains in voltage-gated channels.[27] Two other helices, S5 and S6, are located in the transmembrane region; S6 comprises the inner portion of the pore-forming domain, while S5 comprises the outer portion of the pore-forming domain.[27,28] The first visualization of these helices in addition to the S4-S5 link lead to speculation that the RyR1 structure corresponds to the super family of 6-TM voltage-gated channels for cations, which has been confirmed with the 3.8 Å structure.[26,28] The portion of the S6 domain that confers the cytoplasmic/ion gate (Ile-4937) is the narrowest portion of the ion pore and corresponds to the location of closing and opening. The following figure provides a visual depiction of the different domains of the RyR1 based on color (Figure 2).[24]

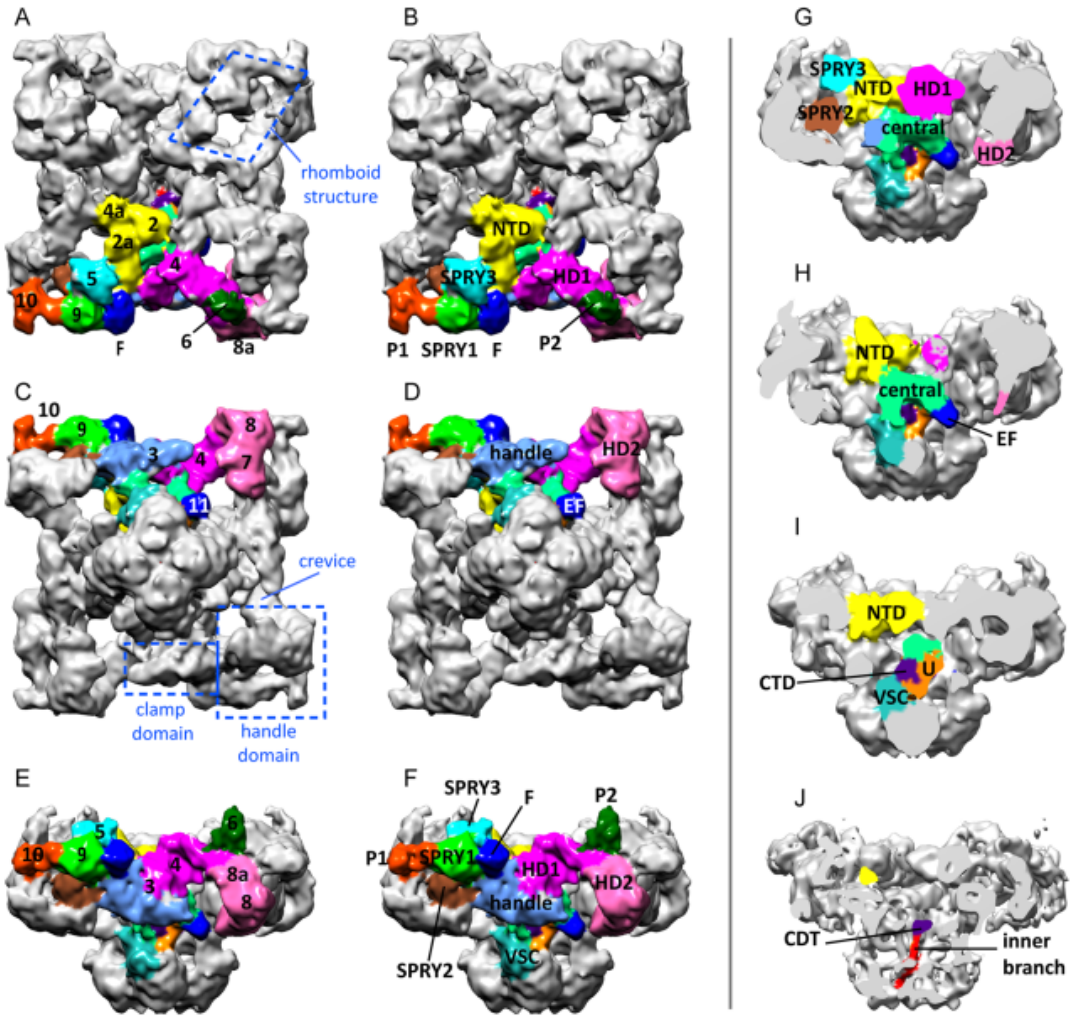

Figure 2. Visualization of the various domains of RyR1 based on color adapted from Samsó et al. (2017)[24]

1.1.5. Binding Partners of the RyR1

There exist a variety of small molecules, and their concentrations regulate the conformation of the RyR1. Ca^{2+} can influence the conformation of the RyR1 through direct effect in the form of direct Ca^{2+} binding or through indirect effect in the form of calmodulin coordination with Ca^{2+} and binding to the RyR1. Activation of the RyR1 by Ca^{2+} has a typical bell-shaped profile; that is, low cytoplasmic [Ca^{2+}] leads to binding at high-affinity Ca^{2+} sites that activate the RyR1,

whereas high cytoplasmic [Ca^{2+}] leads to binding at low-affinity Ca^{2+} sites that inhibit the RyR1.[29] Simultaneously, increased [Ca^{2+}] in the lumen of the SR has been implicated in increased sensitivity to [Ca^{2+}] in the cytoplasmic region. The effect of [Ca^{2+}] on the activation of the RyR1 can be altered by a variety of other reagents including caffeine and ATP. Specifically, caffeine and ATP increase the sensitivity of the RyR1 to Ca^{2+} when the SR load is sufficiently high.[30]

ATP and other adenine nucleotides activate the RyR1 with the most activating being ATP.[31] This activation is, however, modulated by other small molecules such as Mg^{2+}, Ca^{2+}, and dantrolene.[32] ATP, although activating, cannot activate the ryanodine receptor in the presence of Mg^{2+}.[33]

Cytosolic Mg^{2+} at a physiological concentration has been shown to inhibit the RyR1, and a variety of binding sites are implicated. Firstly, Mg^{2+} acts as a competitive antagonist to the high-affinity Ca^{2+} site, and secondly, Mg^{2+} may bind to a low-affinity Ca^{2+} binding sites that controls Ca^{2+} and channel inhibition.[29] With regards to the low-affinity Ca^{2+} binding site, the site is thought to be a non-specific divalent cation inhibitory site that binds Ca^{2+} and Mg^{2+} equally.[34] Interestingly, a third effect is observed in the case of the RyR2. Mg^{2+} was shown to activate the RyR2 at an intermediate [Ca^{2+}], and this was initially attributed to another cytosolic divalent cation binding site.[35] However, a 2014 paper proposed that cytosolic divalent cation binding site was located at a pair of cytosolic EF-hand motifs of the RyR2.[36] Nonetheless, locating this site or the non-specific divalent cation inhibitory site will serve to verify one of these model and provide insight into the emerging role of Mg^{2+} in MH.[37] The following diagram shows the currently accepted Mg^{2+} binding sites with their respective K_A and K_D as well as the ATP binding site (Figure 3).[38]

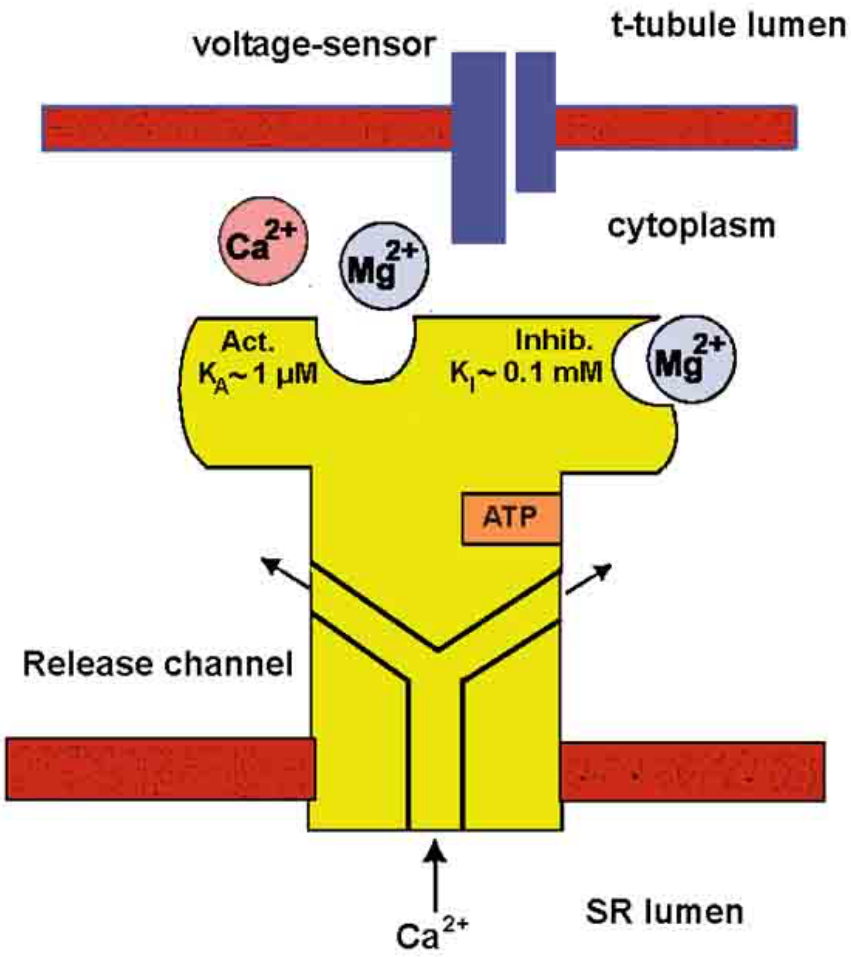

Figure 3. Accepted Mg^{2+} and ATP binding sites of the RyR1 adapted from Smith et al. (1986)[38]

The role of Mg^{2+} in MH has been studied, but recent years have revealed more insight into the relationship. Specifically, a pig model of MH has suggested that the primary dependence of that instance of MH was due to reduced Mg^{2+} inhibition of the channel.[37] Subsequently, a human model showed that reduced Mg^{2+} regulation could cause MH.[39] Furthermore, it was observed in 2017 that dantrolene treatment of MH requires the presence of Mg^{2+} in order to be effective in isolated muscle fibers. 1 mM levels of Mg^{2+} were unable to reduce halothane-induced Ca^{2+} waves; however, increasing the [Mg^{2+}] to 1.5 mM returned dantrolene's ability to decrease the extent of anomalous Ca^{2+} waves. The mechanism of action of dantrolene was previously

unknown, but with this new information, the mechanism is speculated to be through increasing the Mg^{2+} affinity of the RyR1.[40]

There are additionally two proteins that serve as major binding partners for the RyR1, and those are FKBP12 and calmodulin. FKBP12, also known as calstabin 1, associates with each of the four subunits of the ryanodine receptor and typically co-purifies with RyR1.[41] When bound to RyR1, FKBP12 is thought to stabilize the closed configuration under physiological conditions.[42] Without FBKP12 present, the receptor has a higher probability of being found in the open configuration, and the interaction with the ß-subunit of the $Ca_V1.1$ (DHPR) is destabilized.[43] Another binding partner also involved in regulation of the RyR1 is calmodulin (CaM). CaM contains four EF-hand motifs that alter CaM between CaCaM and apoCaM. Both forms of CaM bind with stoichiometry of one CaM to each subunit of the RyR1.[44] The two forms of CaM act as a Ca^{2+} sensor; CaCaM inhibits the RyR1 and SR Ca^{2+} release, whereas apoCaM has been shown to be a partial agonist to RyR1 and SR Ca^{2+} release.[45]

With all these regulators having conformational effects, studying the structure ofryanodine receptor is vital to its understanding. However despite significant effort, successful crystallization of an entire isoform of the ryanodine receptor has yet to occur. Currently, the closest any group has gotten to atomic resolution of the ryanodine receptor has been as a result of cryo-electron microscopy; in 2015, the structure of RyR1 was attained to an overall atomic resolution of 3.8 Å.[21] Recent successes of nanodiscs in cryo-EM with membrane proteins and single-particle reconstructions may be a means of improving this resolution past 3.8 Å.[46]

1.2. Nanodiscs:

1.2.1. Introduction to Nanodiscs

Nanodiscs are small phospholipid bilayers that are able to self-assemble and solubilize membrane proteins by stabilizing the lipophilic transmembrane domain of the protein. An amphipathic, helical protein termed membrane scaffold protein (MSP) is incubated with a phospholipid for a preset duration of time, and the nanodiscs self-assemble when two molecules of MSP wrap around a cluster of phospholipids to form the final product.[46] Verification of the structure of the nanodiscs has been performed; coarse grain and whole-atom molecular dynamics led to a thorough characterization of the nanodisc self-assembly,[47] and small angle x-ray scattering revealed that structure of the nanodisc is, in fact, a phospholipid bilayer with MSP associated at the edge.[48] The figure below shows the structure of the nanodisc from the top and side (Figure 4).[49]

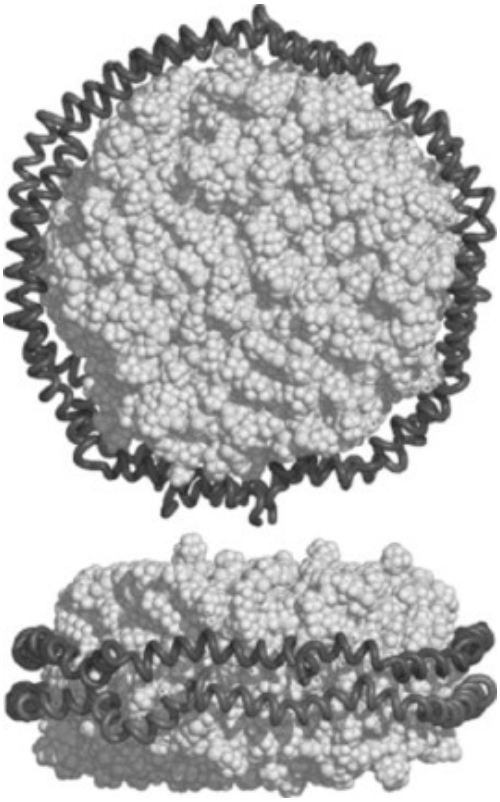

Figure 4. Schematic of the structure of a nanodisc adapted from Ritchie et al. (2009)[49]

1.2.2. Membrane Scaffold Protein

The size of the nanodisc is controlled by the length of the cloned MSP; a variety of commercially available molecules of MSP exist, and one may be chosen to adequately solubilize the membrane portion of the protein. One available type of MSP is called MSP1E3D1; it is sold as bacteria in an agar slab and requires inoculation and purification.[50] MSP1E3D1 is a 277 amino acid, (32,599.98 Da) protein that is similar in sequence to Apolipoprotein A-1 but without the N-terminal domain.[48] MSP1E3D1 contains an additional 3 helical segments for increased nanodisc size, and it yields a nanodisc with diameter of 12.9 nm. The first 21 residues of the protein correspond to the histidine tag and are cleaved by TEV protease leaving a protein of 255 amino acids for use in nanodiscs.[51]

1.2.3. Phospholipids for Use in Nanodiscs

One phospholipid available for commercial use is 1-palmitoyl-2-oleoyl-sn-glycero-3-phosphocholine, or POPC. It is commercially solubilized in chloroform, so it is not usable at that stage; it must be diluted and dried with N_2 gas before ready to use. The structure of POPC is shown in the figure below (Figure 5).

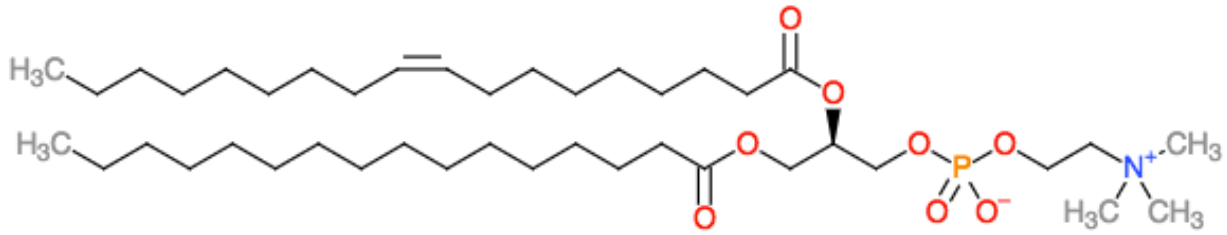

Figure 5. Structure of 1-palmitoyl-2-oleoyl-sn-glycero-3-phosphocholine (POPC)

1.2.4. Nanodiscs Formation and Use

The key to successful incorporation of the receptor into nanodiscs of uniform size is optimization of the phospholipid, MSP, and receptor stoichiometry. One method, based on lipid MSP ratio studies, to determine the correct stoichiometry is defined in the following relationship: $N_L \bullet S = (0.423 \bullet M - 9.75)^2$ where 'N_L' represents the number of lipids per nanodisc, 'S' represents the surface area of each molecule of phospholipid, and 'M' represents the number of amino acids in the membrane scaffold protein.[49] Using the correct, corresponding values, the total surface area of the nanodisc may be predicted. Subtracting the size of the receptor, one may determine the number of POPC needed per two MSP and one RyR1. The ratio is typically expressed as RyR1:MSP:POPC.

In practice, the protein may be purified and stored using detergent; when the protein is ready for study, it may be combined with the self-assembled nanodiscs, and the detergent may be subsequently removed by dialysis. The removal of the detergent serves two purposes; firstly, it returns the protein into an environment more similar to in vivo, and secondly, it diminishes the undesirable effects of the detergent such as absorbance, light scattering, and electron scattering.[46] This proves particularly valuable for cryo-electron microscopy as the electron scattering properties of the detergent may negatively impact the contrast of the electron microscopic image as well as the spread of a sample along the support.[52]

1.3. Introduction to Cryo-Electron Microscopy

1.3.1. Factors Affecting Grid Preparation for Cryo-Electron Microscopy

Once the protein has been introduced into nanodiscs, the sample can be combined with other buffers and reagents to change the configuration. This is of tremendous value as one is able to alter buffer conditions to reflect certain in vivo situations. As one basic example in context of the RyR1, one may alter the buffer of the channel to reflect a open or closed state in order to assess the protein in that specific environment. The sample is then pipetted onto a Quantifoil grid; this grid consists of a carbon or gold support with square shaped holes with each hole covered by a smaller carbon or gold mesh containing minute holes. The grid is blotted to absorb most of the sample, leaving a thin layer of liquid suspended in each of the holes of the holey mesh held by surface tension. The grid is then flash frozen by plunging into liquid ethane cooled by liquid nitrogen; the liquid ethane has a higher heat capacity than liquid nitrogen leading to fast-freezing to vitreous ice and avoidance of crystalline ice formation.

At this stage, a magnitude of different parameters can be changed to alter the resulting cryogenic grid. For one example, the grid may be initially pre-coated with thin carbon to provide a binding scaffold over the holes to localize more sample to that region when the sample is of low concentration. The grid may then also be glow discharged in an effort to increase the hydrophilicity of the grid for sample pipetting. Even another step prior to plunge-freezing could be to pre-saturate with sample in an effort to saturate a large percentage of the non-specific binding sites on the thick carbon scaffolding surrounding the holes.[52] Furthermore, prior to the

plunge freezing one may alter the temperature settings, regulate the humidity of the chamber, and control the blotting force and blotting time.[52] These parameters can both directly and indirectly alter the thickness of the vitreous ice covering the holes in the support film, and the resulting thickness may vary between a few hundred angstroms to a few thousand.[53] The degree of thickness will ultimately be a deciding factor in the highest resolution achieved by the subsequent data processing. Immediately after freezing, the grid may be visualized or stored at liquid nitrogen temperatures.

1.3.2. Technological Advancements in Cryo-EM

Single-particle cryo-electron microscopy has been dramatically advancing in the past decade to the point where the technology has resulted in direct electron detectors (DEDs), gold grids, and electron microscopes the size of a room; however, the technology is still developing. The current electron microscopes receive their radiation source from a variety of electron guns. The three main types of electron guns are as follows: a tungsten tipped filament, a lanthanum hexaboride (LaB_6) tipped filament, and a tungsten field emission gun (FEG). The tungsten tipped filament and LaB_6 tipped filament are thermal filaments that, when heated, expel electrons. The lanthanum hexaboride filament has a lower work function relative to the heated tungsten filament, and consequently, it is more efficient.[54] The most commonly used electron source is the FEG gun because of its high signal to noise ratio and spatial resolution, and it was the first electron source for cryo-EM that achieved a structure below 10 Å.[55] The smaller source size, better beam convergence, and increased brilliance provide a better input to achieve higher resolution structures.[56]

The electrons of the source are accelerated with a voltage varying between 200 and 300 kV for the case of cryo-electron microscopy. The accelerated electrons then pass down the column and through the sample, while they are focused by electromagnetic lenses onto a form of detector.[53] The wavelength of 0.02 Å achieved from a 300 kV voltage source passing to the detector does not currently serve as a resolution limit for electron microscopy as no cryo-EM structures have reached a resolution that low; the limitations arise from factors such as the pixel size of the detector, the levels of background noise, and the fact that electromagnetic lenses are not perfect.[53] Until as recently as 2011, the most conventional methods of data collection have been CCD detectors and photographic film.[57] Although convenient, CCD detectors have lower detective quantum efficiency and, consequently, lower resolution capabilities than film, and despite smaller pixel sizes of CCD detectors, resolution limits have not improved.[58] Since the first 3-D reconstruction achieving atomic resolution in 2011, direct electron detectors have shown much promise.[59] The current electron detectors use monolithic active pixel sensors (MAPS); here, the electrons impact the sensors and pass through semi-conducting membranes, where they are detected by electronic devices.[60] The most current direct electron detectors available for commercial purchasing are the Falcon II and Falcon 3ec from FEI, the K2 Summit from Gatan, and the DE-64 from Direct Electron. As the Falcon 3ec has just been recently introduced to the market, studies have not yet indicated its effectiveness relative to the others. Nonetheless, a 2015 publication regarding the tobacco mosaic virus compared the Falcon II with the K2 Summit using the same microscope with substitutions of the different detector. They found no difference in the resulting resolution or the number of particles required to achieve that high resolution.[61] Taken in context, both can achieve desired atomic resolution; however, the K2

summit has the capability to detect electrons below the pixel size limitation due to its super-resolution capacity.

1.3.3. Radiation Damage from Electron Dosing

When a cryogenic grid is visualized, the grid is exposed to a low dose of electrons that are received by a detector or camera on the other side of the sample. The extent of radiation that results is due to the electron dose, that is the electrons per square Ångstrom.[62] As the magnification increases, the electron dose increases as a consequence, and the sample is exposed to more electrons. To minimize radiation, the sample search is carried out at lower magnification, which supplies the grid with little radiation. The focus and exposure features supply a significantly larger amount of radiation, so as a precaution, the focus step is done on a region adjacent to the area to be exposed. In that way, the exposure is the first large dose of radiation that the specimen is receiving. The damage that results is due to the inelastic collisions of the electrons with the specimen that results in changes at the chemical and physical level.[62] Disulfide bonds are easily the most susceptible to radiation damage as they face the possibility of reduction. In addition, aspartate and glutamate residues also possess a rather large chance of decarboxylation.[63] This illustrates two very different examples of radiation damage; one results from reducing radicals, while the other results from oxidizing radicals.

Although unresolvable, attempts have been made to limit resolution problems resulting from macro level radiation damage; one of the main practices is to collect data as a movie. For example, forty frames of an electron micrograph may be collected over the course of a short time interval in order to take into account any observable movement resulting from ice deformation or particle movement.[64] Using software like MotionCor2 or Unblur, movement vectors for entire

micrographs and for local areas can be determined and used to align frames or particles.[65] Although an essential tool, this correction does not correct chemical changes or particle movement that does not result from electron beam irradiation; instead, one may take an alternate approach of masking specific subdomains on the particle of interest that are known to move little relative to more susceptible regions.

1.4. Image Processing

1.4.1. Pre-Image Processing: Gain and Motion Correction

The software MotionCor2 has several features other than frame/particle alignment that make it that more invaluable.[66] For example, a gain reference can be subtracted from each of the micrographs undergoing motion correction in order to take away the background signal from the detector. Other features available in the software include binning, dose weighting, and frame removal.[66] Binning serves to combine signal from adjacent pixels, which ultimately increases signal-to-noise ratio. Dose weighting takes into expectations of radiation damage at certain voltage, pixel size, and electron dose and attempts to correct for them; however, the micrograph resolution is often compromised as a result. To address this negative consequence, the output is two summed images, one with and one without dose-weighting so that the experimenter may choose. Lastly, one is able to remove frames towards the end or towards the beginning of the movie file. This is particularly advantageous as these are the frames that tend to suffer from radiation damage the most; particularly, the first few frames tend to suffer more from more rapid particle movement, whereas the last few frames may have more macro changes such as ice breaking and protein degeneration.

1.4.2. Pre-Image Processing: CTF correction

The next step following gain correction and motion correction is contrast transfer function (CTF) determination. Although it is not essential at this stage, certain softwares, specifically Relion,

require CTF files present from which it acquires certain inputted microscope parameters (such as pixel size or voltage). The contrast function is defined as follows:

$$\text{CTF}\,(\vec{s}) = -\sqrt{1-A^2}\cdot\sin(\gamma(\vec{s})) - A\ \cdot\cos\big(\gamma(\vec{s})\big) = -\sin(\Delta\emptyset + \gamma(\vec{s}))$$

In the above equation, $\vec{s}$ refers to the spatial frequency, A refers to the amplitude contrast, $\gamma(\vec{s})$ represents the varying CTF phase, and $\Delta\emptyset$ is a global phase shift as a function of amplitude contrast.[67] The contrast transfer function is essentially a quasi-periodic sine function dependent on mostly the defocus setting; it mathematically describes defects in the collected micrographs.[68] The quasi-periodic sine function is visualized by plotting the contrast as a function of the spatial frequency. Higher amplitudes of the CTF (positive or negative) contain high resolution information while the zero values contain no information. Additionally, higher levels of defocus will result in an increased contrast but lower resolution, and lower levels of defocus will result in a decreased contrast but higher resolution.[69] In an effort to find a compromise between the two, one typically collects images throughout a range of defoci; an example of this is depicted below (Figure 6).[70]

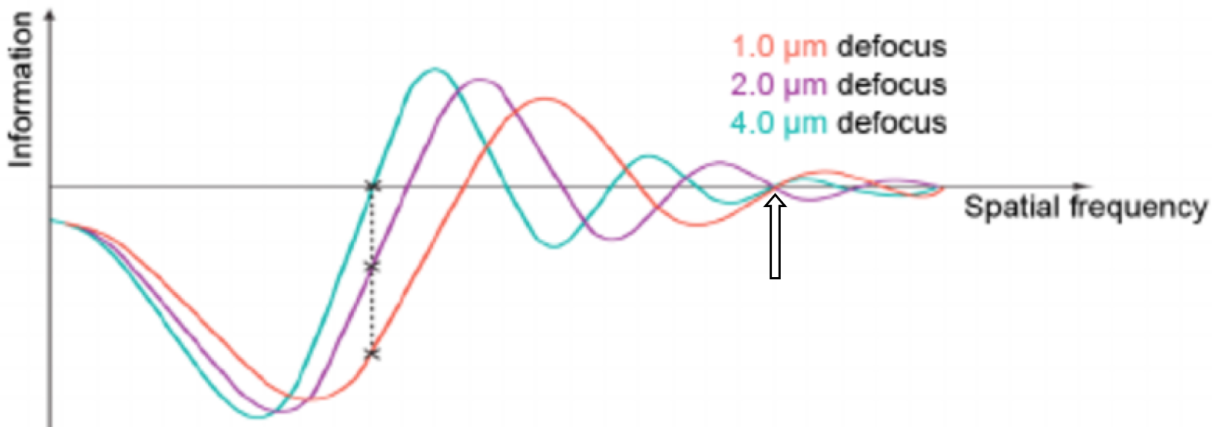

Figure 6. Example of CTF curve with multiple defoci adapted from Ranson et al. (2010)[70]

Of note, the y-axis in this figure is labeled as ‘information’ for clarity, but this is more accurately represented by the label ‘contrast’ or ‘signal-to-noise ratio’ since information cannot be negative. As indicated by the diagram, changing the values of defoci varies the location in which the spatial frequency intersects the x-axis and, as a result, has zero information. By doing so, the areas where the ‘information’ is zero for a given defocus value may differ from the areas where the ‘information’ is zero for another defocus value. Thus if done correctly, the use of different defoci should result in information being present at almost all spatial frequencies. Nonetheless, this is not a perfect system, and sometimes, the different defoci may all have a specific spatial frequency of zero as represented by the white arrow in Figure 6. In this case, the main solution is to collect more images at different defoci to hopefully acquire information at that spatial frequency.

The values of the CTF curves are transformed into Fourier space and the amplitudes are squared to create a power spectrum of each micrograph. The power spectra may then be transformed through rotational averaging to depict the signal-to-noise ratio as a function of spatial frequency. The outcome of these two operations is shown in the figure below with the left panel depicting the power spectrum and the right depicting the rotational average of the power spectrum (Figure 7).[71,72]

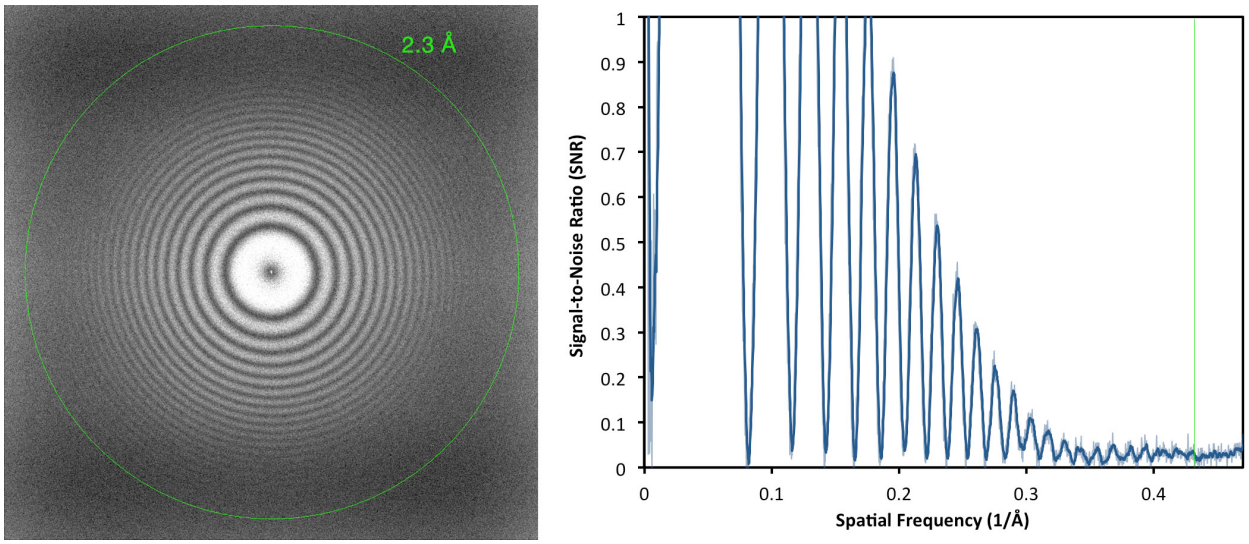

Figure 7. Transformation of CTF into Fourier space adapted from McMullan et al. (2014) and Li et al. (2013)[71,72]

The image on the left shows the power spectrum resulting from transformation of that CTF in Fourier space. The rings shown on the right image are called Thon rings; these are a result of the transformation in Fourier space and provide a more complete visualization of the regions with and regions without information. The white rings in Fourier space correspond to regions of information and the black to regions without information. The center corresponds to low resolution information, and the further the rings expand outwards, the higher the resolution information contained in the initial corresponding micrograph. The figure on the right reflects the pattern of the Thon rings such that the white rings on the left figure correspond to the non-zero values of SNR and the black rings on the left figure correspond to zero values of SNR. The green circle on the left figure and the green line on the right figure depict the area where the Thon rings no longer appear, and that is the resolution limit.

These power spectra may be determined using a multitude of computer softwares including Gctf, ctffind3, and ctftilt. For CTF correction, the power spectra are then matched with Thon rings from standards of different defoci to predict each micrograph's true defocus. The determined

defoci values will then be used in 3D reconstructions and refinements to improve the resolution through averaging of information from the non-zero regions of the CTF rather than accidental averaging of noise. In addition, the Fourier transformation can visually depict other anomalies including astigmatism, crystalline ice, and drift. Although these may not be corrected through CTF corrections, the information may be used for decisions regarding discarding bad micrographs.

1.4.3. Image Processing: Particle Picking and Relion

Following the pre-processing, the micrographs are introduced into a variety of softwares for particle picking and subsequent steps. The pathways diverge based on personal preferences and even computational power, so the following discussion will diverge to reflect the two routes.

EMAN2 is written in C+++ and is able to take a microscopy data set to a 3D reconstruction beyond 10 Å.[73] It offers a user-friendly GUI software, Boxer, for particle picking that allows easy importation into other softwares such as Relion and Spider. A relatively small amount of particles may be picked and their coordinates submitted for 2D classification in Relion. The preliminary 2D classification provides references for an autopicking algorithm in Relion.[74] The autopicking selects particles on the already selected micrographs and the remainder of the micrographs. The resulting particles may be resubmitted for 2D classifications and the bad classes removed until the data set is considered polished. Or, one may manually deselect the bad particles and select any particles missed by the autopick. In either route, these particles should be submitted for 3D classification to generate classes for user analysis. From these classes, the user may remove any particles that may be in an alternate conformation than the major or desired conformation.

The selected class can then be submitted for 3D refinement; this method splits the data into two halves, creating a volume for each half and generating correlation coefficients for the two volumes. The result is a Fourier shell correlation (FSC) curve.[75] Different criteria are used for selecting the final resolution. The most common practice is to select the resolution at the spatial frequency where the FSC curve has a value of 0.5, but other choices of value are used. For instance, a value of 0.33 corresponding to a SNR of 1.0 and a value of 0.143 derived from a value used in X-ray crystallography are also used in practice.[76] Below is an example of resolution determination using a FSC value of 0.5 (Figure 8).[77]

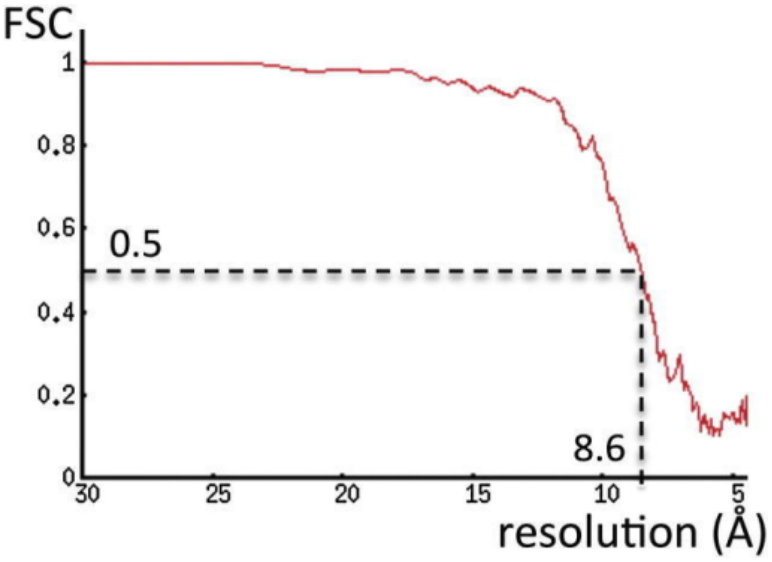

Figure 8. Example of resolution determination using an FSC value of 0.5 adapted from Maurer et al. (2012)[77]

1.4.4. Image Processing: Spider and Frealign

Another alternate route is through spider and, subsequently Frealign since Frealign only has 3D reconstruction capabilities.[78,79] Following the boxer particle picking stages, the coordinates are brought to Spider, re-centered, and extracted from the original micrographs (in spider format).

The extracted particles may then go through two different routes. Firstly, the particles may be inverted and compared to a reference in a variety of different rotations for 2D classification. This differs from the Relion software in multiple aspects. Firstly, Relion provides unbiased, reference-free classifications that minimizes noise fitting; however, the different angles of the references provide for better classification as each particle is compared to all the specified angles of the reference that takes place in spider. This classification proves useful if the particles selected may be verified as actual particles rather than non-particles, but if this is not the case, the "Einstein from noise phenomenon" may occur. This occurs when random, pure noise is fit into the given references and averaged; the resulting images tend to look like the reference but only because the chosen features from the noise are averaged to look like the references.[80]

Although useful, these 2D projections are not necessary for 3D reconstruction of the data set. Instead, the particles may be submitted to the 3D as either a stack for Spider or as document file referencing the actual particles for Relion. Both softwares have relatively similar capacities; Spider is able to perform 3D classifications and 3D refinements, and Relion is able to do the same. The 3D classification serves as a means of separating particles belonging to different conformations. For example, if a channel such as the RyR1 is in a conformation between open or closed or is in a minority conformation, those particles may be classified separately and removed from the stack or reference file to leave only all the particles of the desired conformation. These particles can be submitted for 3D refinement, and the 3D structure based on the input particles will be refined until no resolution improvements occur.

1.4.5. Post-Image Processing: Rosetta and Phenix for Map Building

Once a sufficient resolution is achieved, the volume can be submitted to a model building software such as Phenix or Rosetta. Rosetta has a variety of functions for model building, but the de novo structure prediction algorithm serves as a good map building software.[81] Specifically, Rosetta inserts backbone fragments using low-resolution energy function and sampling approaching to survey for proper fitting. An atomic-detail refinement mode is available that may bring the structure to the best match of each atom to the volume. Rosetta additionally offers the ability for the user to fit some portions of the structure as an initial guideline for the software to align the structure.

1.5. Future of Cryo-Electron Microscopy: Increasing Use and Applications

The incidence of determined cryo-EM structures has increased exponentially since 2010 and membrane proteins comprise a higher percentage of the structures determined by cryo-EM than they do for NMR or X-ray crystallography; this is depicted in the figure below (Figure 9).[82]

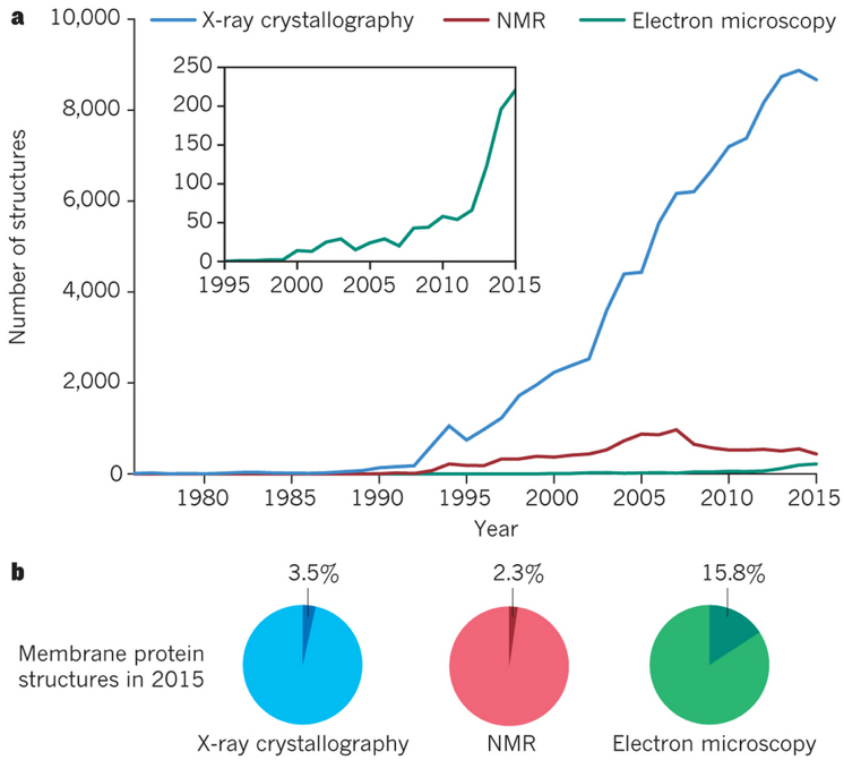

Figure 9. Growing incidence of electron microscopy for structure determination adapted from Fernandez-Leiro et al. (2016)[82]

With structures reaching ~3.0 Å resolution from cryo-EM, it is becoming a real contender to X-ray crystallography. This year (2017), the average resolution for structures desposited in the EMDataBank from single particle cryo-EM was 7.9 Å; this is the first year that this average has

fallen below 10 Å, and the trends of resolution for this year and previous are displayed in the figure below (Figure 10).[83]

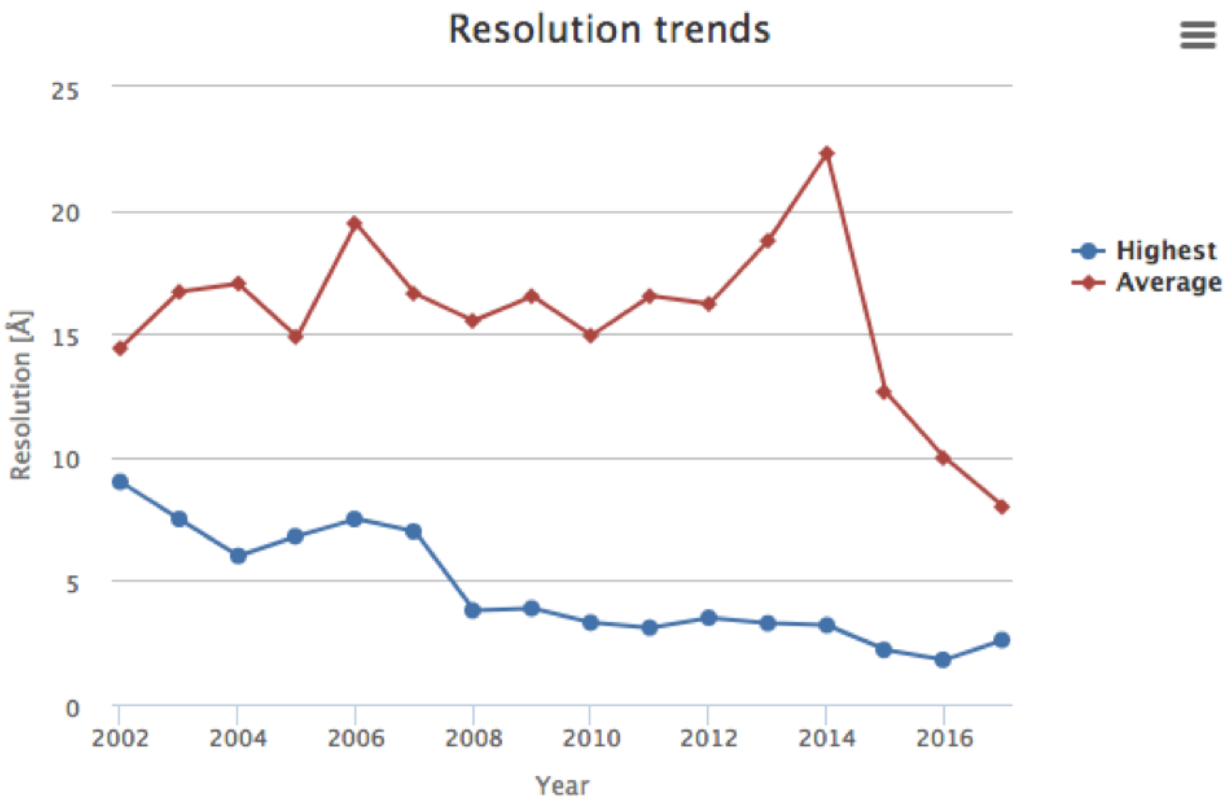

Figure 10. Resolution trends of single-particle structures deposited in EMDataBank adapted from Lawson et al. (2016)[83]

Lastly, the result from cryo-EM is not binary; that is, low resolution volumes resulting from cryo-EM still result in an informative result, whereas X-ray crystallography depends entirely on successful crystallization of a protein.[84] With the growing incidence of cryo-EM facilities, protocol changes to effectively increase resolution, and improving technologies, cryo-EM will eventually achieve resolutions below 3.0 Å. In addition, cryo-EM will prove invaluable as it progresses because it provides more natural protein environments than crystals and allows the user to manipulate the state through altering of buffer conditions.

1.6. Goals and Aim of Study

The initial goal of the study was to insert the RyR1 into nanodiscs for a number of reasons. Firstly, the nanodisc will return the RyR1 from a detergent environment to a more native membrane environment. Secondly, the lack of detergent will theoretically improve the resolution of the images collected during a subsequent cryo-electron microscopy phase.

Following preliminary verification of successful incorporation of the RyR1 into nanodiscs, the aim of the study was to assess the conformation of the ryanodine receptor from skeletal muscle (RyR1) in response to additions of Mg^{2+} and AMP-PCP using single-particle cryo-electron microscopy and subsequent 3D reconstruction. These additions serve to mimic resting physiological conditions with AMP-PCP replacing ATP because it is a non-hydrolyzable analog. Since ATP is activating and Mg^{2+} is inhibiting, the expected conformation is not perfectly clear; however, it is postulated that the channel will be closed as it is closed in resting physiological conditions. The resulting closed model of RyR1 is expected to serve as a more accurate depiction of the true closed state of the RyR1 because it is the result of buffer conditions more similar to the cell contents that the RyR1 would experience in vivo.

2. Methods

2.1. Purifications

2.1.1. Rabbit Tissue Extraction and Sarcoplasmic Reticulum Vesicle Isolation

A rabbit is anesthetized with a mixture of ketamine, xylazine, and acepromazine; the dosing for each of these is 35 - 50 mg/kg, 5 - 10 mg/kg, and 0.75 - 1.0 mg/kg, respectively. When the rabbit does not respond to pinching, its heart is removed, and it is exsanguinated. The rabbit's body is placed on ice and the skin removed from the rabbit. The back muscle and the muscle from the hind legs is removed from the rabbit, cut into one inch by one inch pieces, and flash-frozen in liquid nitrogen. When ready for use, 130.0 g of frozen tissue is weighed and pounded with a hammer until broken into small pieces. The muscle is homogenized in a commercial blender with 170 mL of 0.3 M sucrose and 5 mM imidazole-HCl buffer at pH 7.4 per 50.0 g of tissue, in this case 442 mL. The homogenization is done for three 30 second intervals with 20 second intervals in between. The homogenate is centrifuged at 8000 rpm using a 510BCl-500γ rotor for 21 minutes. The supernatant is discharged, and the pellet containing the SR vesicles is resuspended in a commercial blender with fresh 170 mL of 0.3 M sucrose and 5 mM imidazole-HCl buffer at pH 7.4 in the same manner as described previously.

The rehomogenates are centrifuged at 8000 rpm using a 510BCl-500γ rotor for 27 minutes; in this instance, the soft pellet is discarded by passing the supernatant is passed through 8 layers of cheese cloth. The filtered homogenate is centrifuged at 43,5000 rpm in a Beckman Ti 45 rotor

(220,000 g) for 50 minutes to pellet the SR vesicles. The resulting pellet is suspended in 0.3 M sucrose and 5 mM imidazole-HCl buffer at pH 7.4 at a ratio of 1.5 to 2.0 mL per 250 mL equivalent of filtered homogenate. The resuspension is aliquoted into 500 µL fractions and flash-frozen in liquid nitrogen for storage at -80ºC.

The concentration of the vesicles is determined by a Bradford method. Standards of BSA diluted to concentrations of 0.01, 0.03, 0.05, 0.07, and 0.09 mg/mL with water are mixed with equal parts Bradford reagent, and the absorbance is measured at 595 nm to generate corresponding data points. A standard curve best representing the acquired data points is determined with a linear or logarithmic fitting software in Microsoft Excel; an R^2 value of 0.95 or higher is considered adequate to use for concentration determination. The vesicles are diluted in water to a concentration between 0.01 and 0.09 mg/mL and combined with equal parts Bradford reagent. The absorbance at 595 nm is determined and used in the equation generated from the BSA standards to give a value of concentration for the vesicles.

2.1.2. RyR1 Isolation from Sarcoplasmic Reticulum Vesicles

Approximately 70 mg of vesicles are thawed in a 37ºC heating block and placed on ice. Buffer stocks are added in the following order to attain the following concentrations: water, 1M NaCl, 20 mM MOPS, 2 mM DTT, 0.025 mg/mL aprotinin and 0.025 mg/mL leupeptin and 0.0125 mg/mL pefabloc SC as a cocktail, vesicles, and 8.8% CHAPS with 0.6% phosphatidylcholine (PC) as a cocktail. The mixture is stirred vigorously on ice for 15 minutes until the solution no longer appears turbid, and the SR vesicles are solubilized. The solution is centrifuged at 43,000 rpm in a TLA 100.3 (100,000 g) for 60 minutes, and the pellet is discarded. Approximately 3 mL of the solution is loaded into a 34 mL discontinuous sucrose gradient consisting of 5 mL 20%

sucrose, 6 mL 18% sucrose, 6mL 16% sucrose, 6 mL 14% sucrose, 6 mL 12% sucrose, and 5 mL 10% sucrose with a peristatic pump. The gradient is centrifuged at 27,000 rpm using a SW32 rotor (141,000 g) at 4ºC with low braking and low acceleration for 18 to 24 hours to separate the RyR1 from contaminant proteins. The gradient is unmounted from the top and collected in 1.5 to 2 mL fractions. Every other fraction is ran combined with 2 equivalents of 3X SDS loading buffer (containing ß-mercaptoethanol) on a 12.5% SDS-PAGE gel to check the location of the RyR1 at 80-120 V until the gel front runs off, approximately an hour to an hour and a half. The gels are stained with coomassie blue and the peak fractions containing RyR1 pooled.

The peak fractions are diluted 5 fold in buffer to a final concentration of 20 mM Na-MOPS at pH 7.4, 0.5% CHAPS, 2 mM DTT, and 0.025 mg/mL aprotinin and 0.025 mg/mL leupeptin and 0.0125 mg/mL pefabloc SC as a protease inhibitor cocktail. A 1 mL prepacked HiTrap Heparin column is prepared with filtered water followed by 10 mL of equilibration buffer consisting of 0.2 M NaCl, 20 mM Na-MOPS at pH 7.4, 0.50% CHAPS, 2 mM DTT, and 0.025 mg/mL aprotinin and 0.025 mg/mL leupeptin and 0.0125 mg/mL pefabloc SC as a protease inhibitor cocktail at a rate of 1 mL/min. The diluted fractions are loaded at a speed of 0.5 mL/min overnight, and the column is then washed with mL of the equilibration buffer. The RyR1 is eluted with an elution buffer consisting of 0.9 M NaCl, 20 mM Na-MOPS at pH 7.4, 0.50% CHAPS, and 0.025 mg/mL aprotinin and 0.025 mg/mL leupeptin and 0.0125 mg/mL pefabloc SC as a protease inhibitor cocktail, and it is collected in fractions of 150 µL fractions. The Heparin column serves to concentrate the RyR1 into peak fractions. 5 µL of each fraction is combined with 10 µL of Bradford reagent on a piece of Parafilm assess the peak of the elution. The peak elution fractions are pooled, and the subsequent fractions are also pooled in a separate tube. Each pooled fraction is then assessed for protein concentration by the Bradford method

described above. The pooled fractions are then aliquoted into 15 μL aliquots and frozen in liquid nitrogen; these fractions are labeled and stored at -85ºC. 5 μL of the fractions is saved for negative staining.

2.2. Negative Stain: Assessing the Quality of the Purified Ryanodine Receptor

A carbon film-coated grid is glow-discharged with 25 mA for 25 seconds. 5 µL of sample from the peak fraction is pipetted onto the carbon film-coated grid and allowed to incubate for 60 seconds. The liquid is then blotted with filter paper. The grid is then washed twice with water for 2 seconds with blotting following each rinse. The grid is then washed once with 0.75% uranyl formate for 2 seconds, blotted with filter paper, washed again with 0.75% uranyl formate for 20 seconds, and blotted for a final time. The grid is then stored until visualization is desired. When ready for visualization, the grid is loaded into a TEM Tecnai F20 and images are collected with a defocus range of 1.0 µm to 2.0 µm. These images are used to assess the quality of the ryanodine receptor.

2.3. Nanodiscs: Formation

When the sample is ready to be solubilized into nanodiscs, the 15 µL fractions are thawed in a 37ºC heating block until no ice is present. The ratio of RyR1 to MSP to POPC is calculated using the equation $N_L S = (0.423M - 9.75)^2$, where N_L is the number of molecules of phospholipid (POPC), S is the surface area of the phospholipid, and *M* is the number of residues in the molecule of MSP. A variety of ratios close to the calculated ratio are empirically tested to ultimately determine the best ratio by visual interpretation through electron microscopy. The POPC is prepared by taking 5 µL of POPC stock in chloroform, drying it with N_2 gas, and diluting it 20 fold in buffer to final concentrations of 20 mM Na-MOPS at pH 7.4, 900 mM NaCl, 2 mM DTT, and 0.5% CHAPS. The appropriate amount of this buffer is added to the microcentrifuge tube to reach the desired volume followed by the determined amounts of POPC, MSP, and then RyR1 to reach the desired ratio and concentrations. The solution is allowed to incubate on ice for 90 minutes to allow for formation of the nanodiscs.

After incubation, 60 µL of the nanodisc mixture is pipetted into a 50 µL dialysis button to form a liquid dome at the dialysis interface. A dialysis membrane with a molecular weight cutoff of 6,000 to 8,000 is placed over the opening of the button, and a rubber O-ring is used to fasten the membrane into place. The dialysis buttons are placed into 250 mL of dialysis buffer consisting of 20 mM Na-MOPS at a pH of 7.4, 855 mM NaCl, and 2 mM DTT. The buffer is replaced after 4 hours and then allowed to continue dialyzing overnight in fresh buffer. The button is then removed from the buffer and the membrane cut with a razor blade. The 50 µL of nanodisc solution remaining in the button is extracted with a pipette and placed on ice. 5 µL of the

nanodisc solution is stained with uranyl formate as described previously to ensure that the ryanodine receptor still has its structural integrity.

2.4. Cryo-Electron Microscopy Protocol

2.4.1. Grid Preparation Protocol for Cryo-Electron Microscopy

The RyR1 nanodiscs are combined with buffers to a final concentration of 2 mM EGTA, 5 mM AMP-PCP, 2 mM Mg^{2+}, 20 mM MOPS, 1.2 mM DTT, 500 mM NaCl; there is no detergent remaining in solution following dialysis. The sample is ready for freezing at this stage. Four to eight Quantifoil grids are washed in water, then acetone, then isopropanol, then chloroform. The grids are glow discharged at 15 mA or 25 mA for 25 seconds. 3.5 μL of sample is pipetted onto the grid and allowed to incubate for 60 seconds as a pre-saturation method. The grid is then blotted using filter paper and pressure applied with the fingers. The grid is loaded into the Vitrobot with varying blot force, blot time, and temperature, and it is then plunge frozen into liquid ethane. The grid is then transferred to liquid nitrogen for storage.

2.4.2. Micrograph Acquisition

When ready to be visualized, the grid is placed on the pre-cooled holder and loaded into the Tecnai F20 with a CCD camera. Images are collected with a defocus range of 1.5 μm to 3 μm, and these images are used to assess the quality of the vitreous ice and the ryanodine receptor. Once the sample contains a sufficient concentration and quality, the remaining grids are loaded into a Titan Krios with a K2 summit direct electron detector, and images collected with a defocus range of 1.0 μm to 2.0 μm to attain a thorough data set. The magnification is set to 105,000 resulting in a pixel size of 1.39 Å with a super resolution of 0.7 Å. The targeted total dose is set

to 40 electrons/Å^2 with a targeted dose rate of 1-8 electrons/pixel/second and a dose per frame of 1-2 electrons/frame. The images are saved in movie format (40 frames) without the gain reference subtracted.

2.4.3. Image Processing Protocol

The images were unzipped to a computer containing a Linux based operating system, and the gain reference is rotated 270 degrees and subtracted from each image through the software Motioncorr2. Simultaneously, Motioncorr2 corrects for motion of each 5x5 patch and truncates the first two and last three frames of the movie files. CTFFIND3 and GCTF are used to determine the actual defocus values for later correction. Particles are picked on the first half of the micrographs using the software Boxer by EMAN2. These particles are provided to the software Relion, where they are extracted and sent for 2D classification into 50 classes. The classes are assessed and selected to be given as references for autopicking. Autopicking is performed on the remaining micrographs, 1041 through 2083. These picked particles are all visualized using Relion, and the non-particles (false positives) selected by the autopick algorithm are manually removed. The particles are then combined with the particles picked from Boxer and sent again for 2D classification of 50 classes. The particles from the best classes are selected for 3D classification with 2 different classes. Simultaneously, the combined particles are sent to Spider for a reference-based 2D classification. The particles are also stacked using Relion, and sent to Frealign for 3D classification as well.

3. Results

3.1. Protein Purification Results

3.1.1. Sarcoplasmic Reticulum Vesicle Concentration Determination

Sarcoplasmic reticulum vesicles were purified using the protocol described above, and the concentration of the resulting vesicles was determined using the Bradford assay described above. Figure 11 below serves as an example for the resulting Bradford standard used to determine the concentration of the SR vesicles.

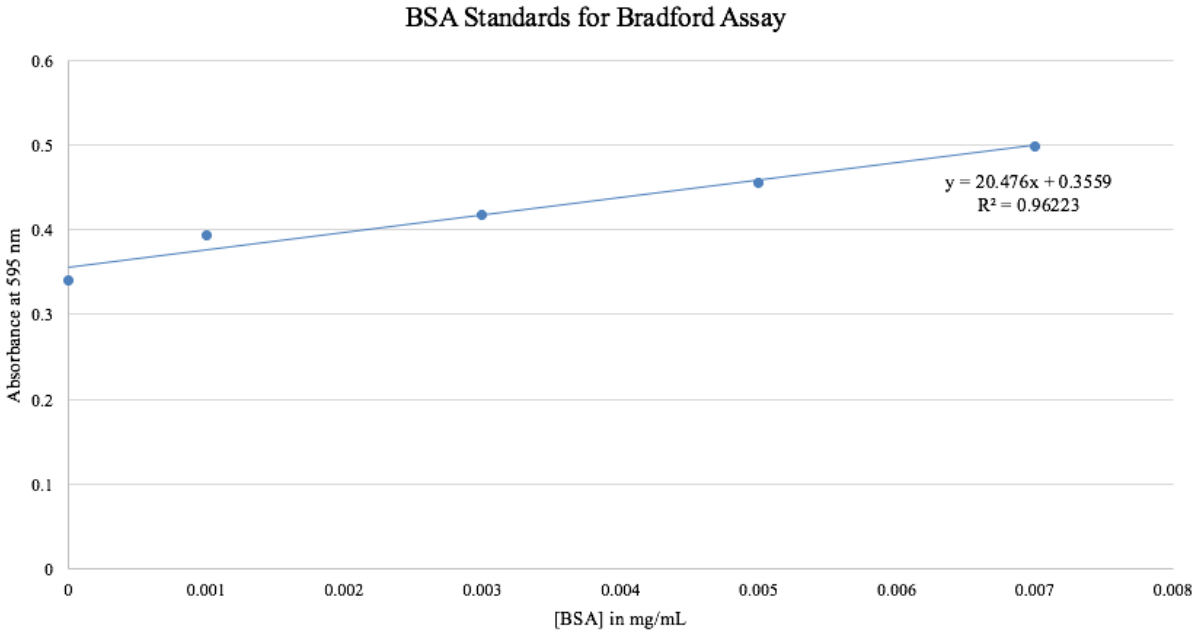

Figure 11. Absorbance at 595 nm as a function of [BSA] to generate a standard curve to determine sarcoplasmic reticulum vesicle concentration following tissue extraction.

In this particular incidence, the concentration of the protein present in the SR vesicles was determined to be 54 mg/mL from an absorbance value of 0.466 at 595 nm from the 10,000-fold diluted sample (Figure 11). Ranges of concentrations varied from approximately 25 mg/mL to 60 mg/mL based on the amount of buffer used to solubilize the pelleted vesicle fraction. The determined concentration is then used to assess the amount of CHAPS for adequate solubilization.

3.1.2. Sucrose Gradient Separation

Following vesicle purification and sucrose gradient separation, fractions from deconstructed sucrose gradients are ran on an SDS-PAGE gel; an example gel is shown below (Figure 12). The gel is used as an analytical method in order to determine the purest fractions to be pooled for concentrating with a Heparin column.

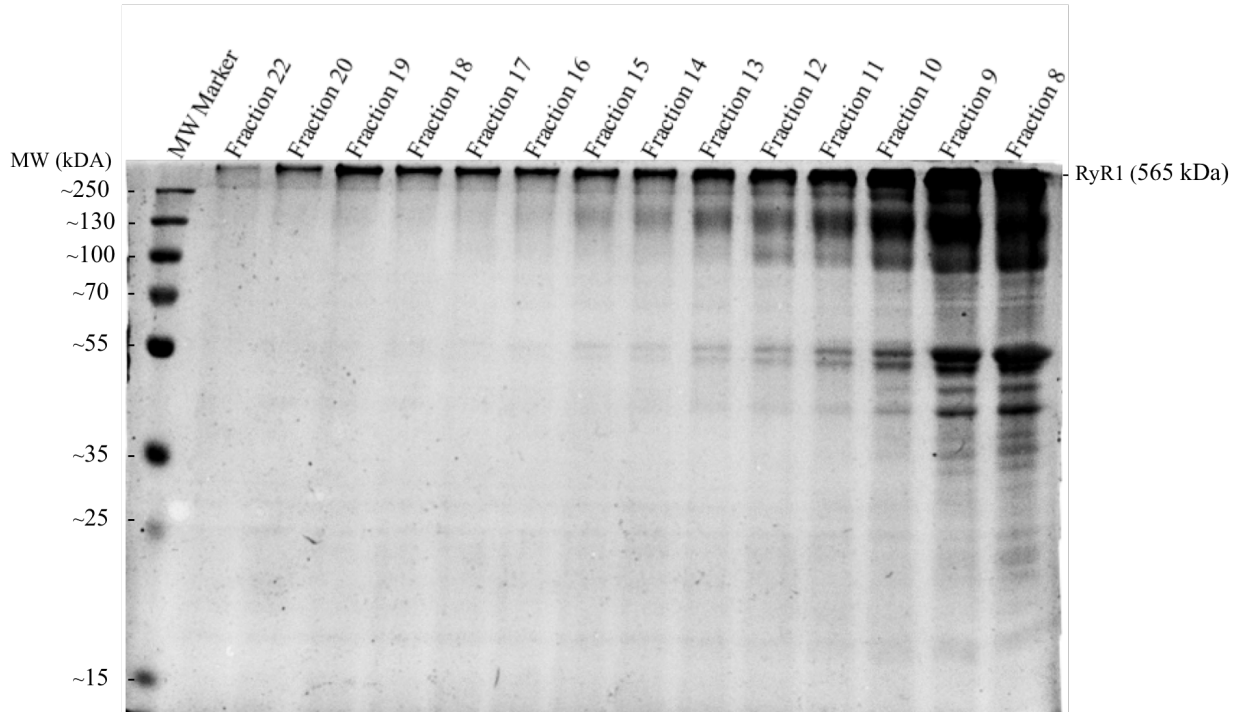

Figure 12. SDS-PAGE gel consisting of fractions from a sucrose gradient used in RyR1 purification from sarcoplasmic reticulum vesicles

3.1.3. RyR1 Concentration Determination

At the end of purification, the concentration of the protein is determined in order to properly optimize the ratio needed for formation of nanodiscs; below is an example of the Bradford assay and standard used to determine the protein concentration (Figure 13).

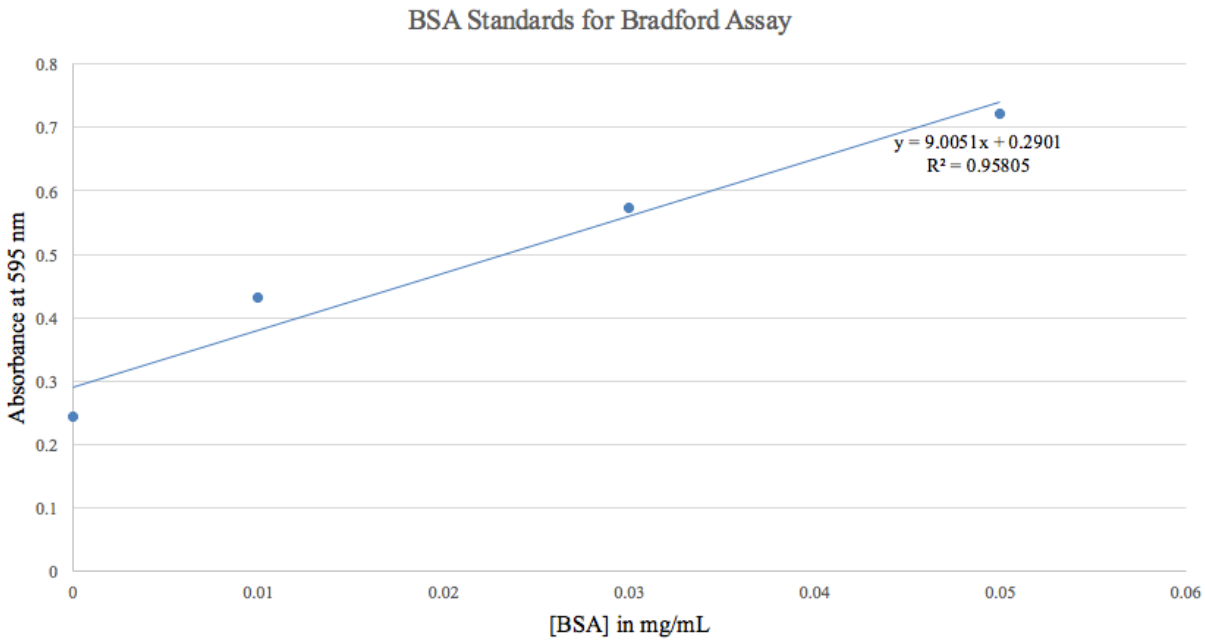

Figure 13. Absorbance at 595 nm as a function of [BSA] to generate a standard curve to determine protein concentration following RyR1 purification

In this particular incidence, the concentration of the vesicles was determined to be 1.5 mg/mL from an absorbance value of 0.433 at 595 nm from the 100-fold diluted sample. Throughout different purifications, ranges of concentrations of RyR1 varied from approximately 0.5 mg/mL to 5 mg/mL. Using this value, a given concentration of protein may be accurately used, and the desired ratio of MSP and POPC for formation of nanodiscs may be properly achieved.

3.2. Incorporation of RyR1 into Nanodiscs Results

3.2.1. Determination of Optimal Ratio

$$N_L \cdot S = (0.423 \cdot M - 9.75)^2$$

A value of 255 for 'M,' corresponding to the number of amino acids in the MSP1E3D protein following cleavage, is substituted into the equation above. N_L • S, or the area of the nanodisc is determined to be 9626 $Å^2$. Subtracting the area of the transmembrane region of the RyR1, 6400 $Å^2$, the area remaining that needs to be occupied by POPC is determined to be 3226 $Å^2$. Dividing by a value of 70 $Å^2$ for 'S,' corresponding to the surface area of each molecule of POPC, the number of POPC theoretically needed to solubilize the RyR1 is determined to be 46. Thus, the calculated theoretical ratio of RyR1:MSP:POPC should be 1:2:46.

3.2.2. Addition of EGTA , Mg^{2+}, and AMP-PCP for Open-State/Physiological Conditions

With careful use of the Ca/Mg/ATP/EGTA Calculator v1 constants from Theo Schoenmakers' Chelator, the optimal amount of EGTA for addition was determined in order to maintain a physiological level of Mg^{2+} while limiting Ca^{2+} to a resting and minimal level. The following figure (Figure 14) shows the output from the calculator. [85]

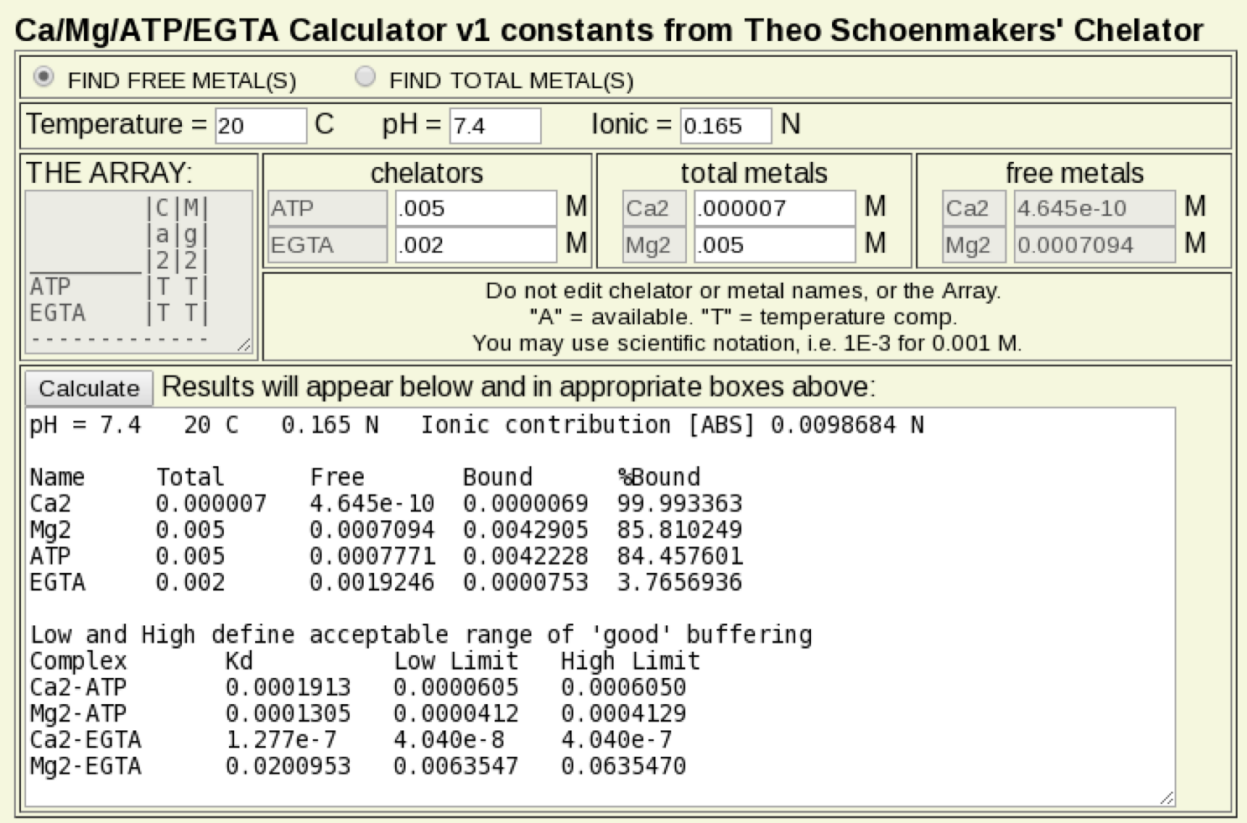

Figure 14. Output from Ca/Mg/ATP/EGTA Calculator v1 Constants from Theo Schoenmakers' Chelator using values to optimize desired concentrations for cryo-EM adapted from Schoenmakers et al. (1992)[85]

The value of 0.007 mM Ca^{2+} was estimated for the amount of Ca^{2+} present in the deionized water used in the laboratory. Using the calculator, it was determined that 0.002 M EGTA will chelate 99.99% of the Ca^{2+} bound in the water. A value of 5.0 mM Mg^{2+} will achieve a value of 0.778 mM free Mg^{2+}, which matches the physiological value of 0.7 to 1 mM free Mg^{2+}.[86,87] In addition, these final values will ensure adequate supply of both small molecules so that the receptor may bind both readily. AMP-PCP, a non-hydrolyzable analog of ATP, is substituted in place for ATP. The structure of AMP-PCP is depicted below (Figure 15).

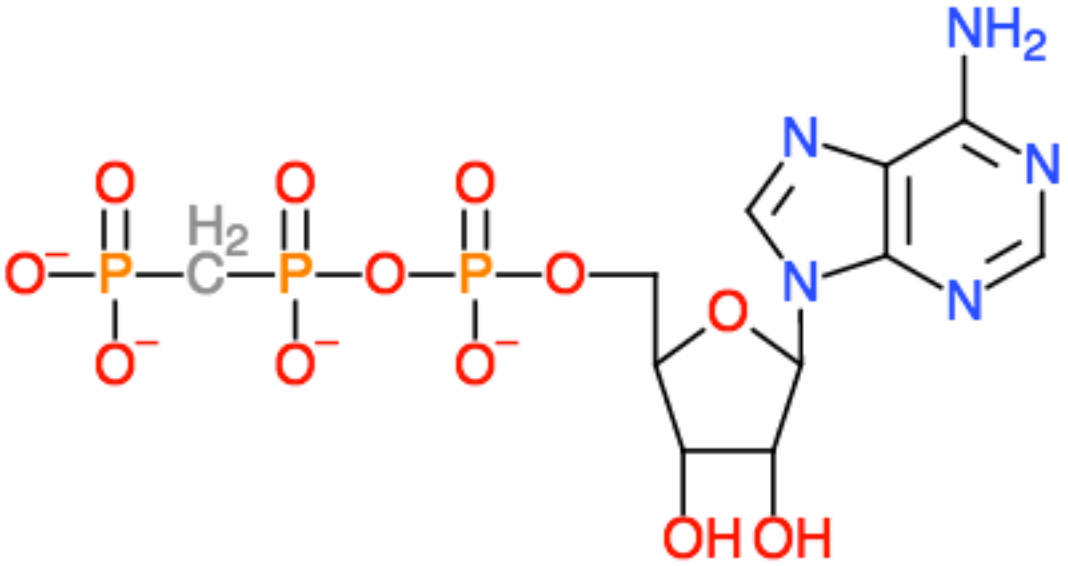

Figure 15. Structure of AMP-PCP, a non-hydrolyzable analog of ATP

3.3. Negative Stain for Nanodisc Analysis

3.3.1. RyR1 Nanodisc Insertion Confirmation

Following dialysis, no detergent remains in the solution. This would, theoretically, lead to protein aggregation or degradation if no means of transmembrane stabilization is present. This gives rise to a preliminary means of conformation that the ryanodine receptor is inserted nanodisc; if the receptor holds its structural integrity, then the receptor is likely stabilized by the nanodisc. Below is an example of negative stained micrographs before and after nanodisc solubilization at the ratio of RyR:MSP:POPC as 1:2:36. (Figure 16)

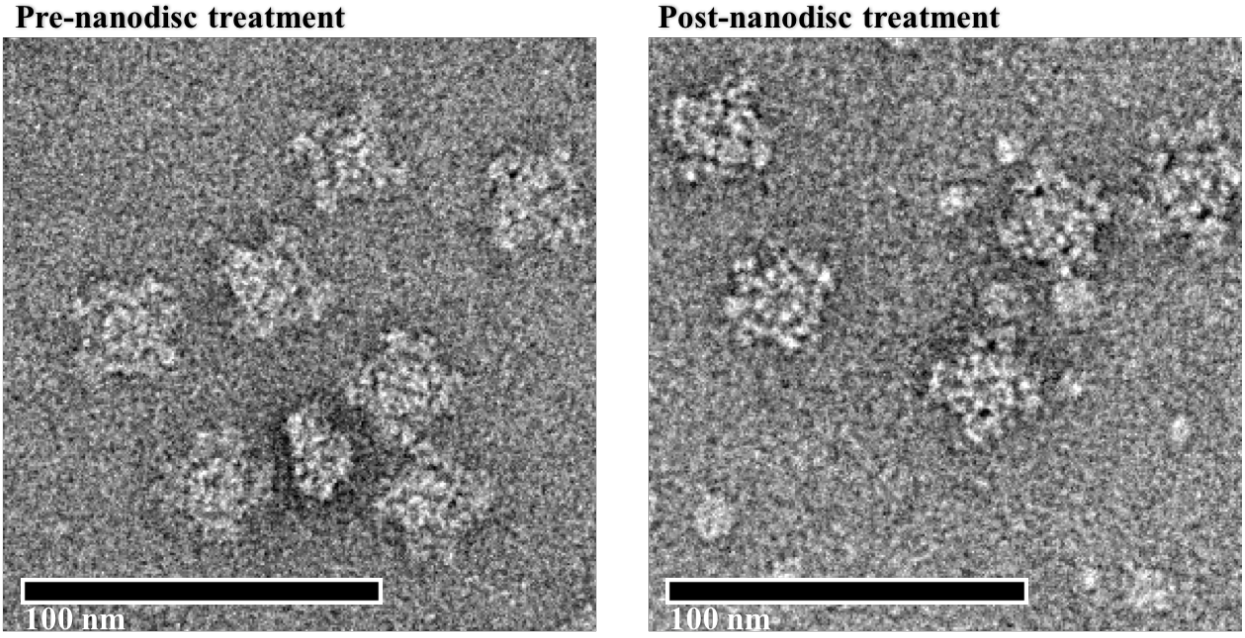

Figure 16. Comparison of pre and post nanodisc treatment

In both the image on the left and the image on the right, the receptor retains its square conformation and structural integrity; since the image on the right is without detergent, it appears the nanodisc successfully stabilized the transmembrane region of the RyR1.

3.3.2. Comparison of RyR1 Nanodisc Ratios 1:2:36, 1:2:50, 1:2:70, and 1:4:72

With the theoretically determined ratio of 1:2:46, four ratios of RyR1:MSP:POPC were elected for testing and negative staining analysis. These ratios were 1:2:36, 1:2:50, 1:2:70, and 1:4:72. Selected regions of micrographs from each ratio are displayed in the figure below for comparison (Figure 17).

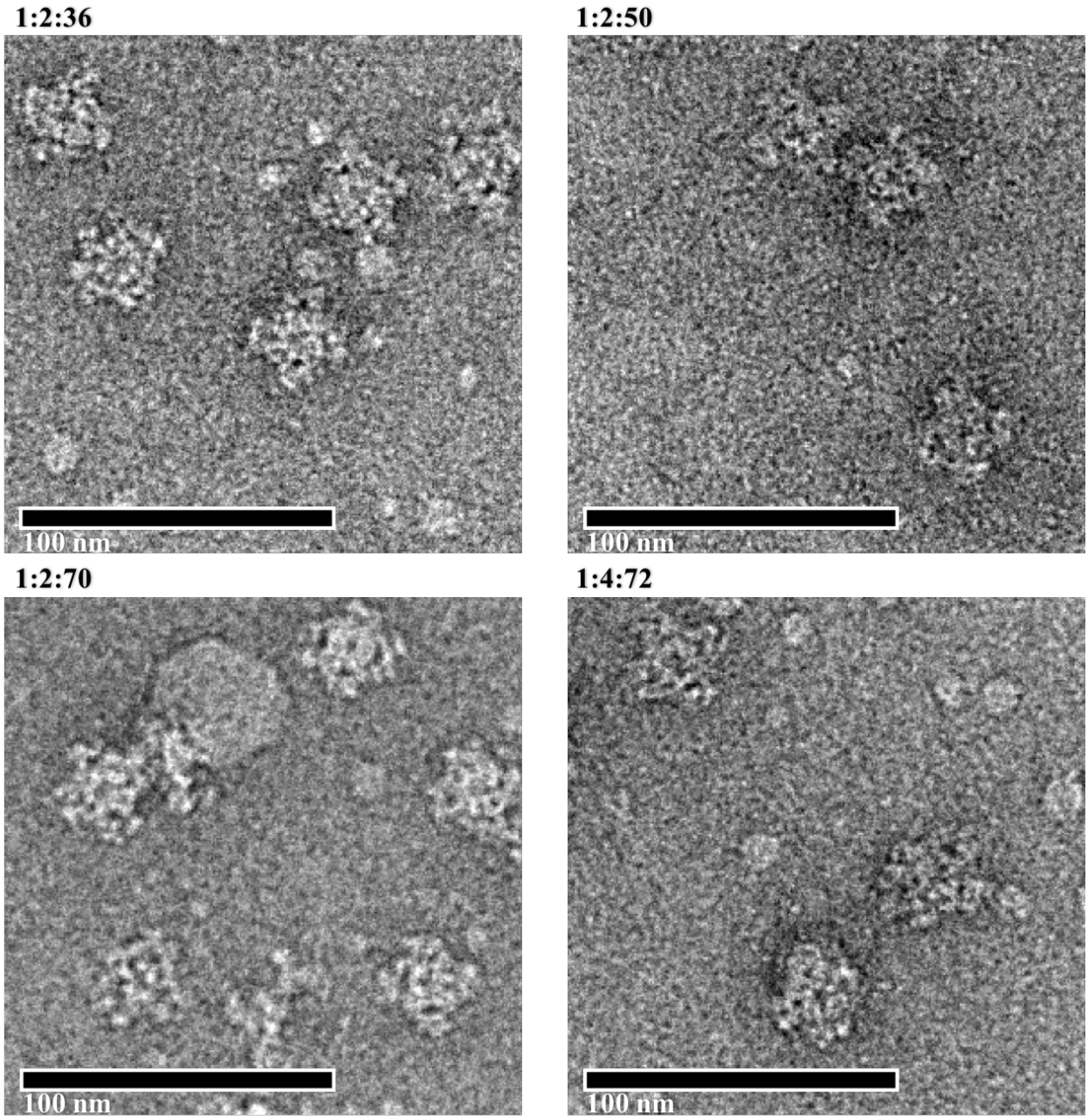

Figure 17. Negative stain depiction of nanodisc ratios (RyR1:MSP:POPC) of 1:2:36, 1:2:50, 1:2:70, and 1:4:72

Both the nanodisc ratios (RyR1:MSP:POPC) of 1:2:36 and 1:2:50 proved sufficient for solubilizing the RyR1, but the ratio of 1:2:50 agrees more closely with the theoretical ratio and was elected for use. The ratio of 1:2:70 resulted in large accumulations of lipids, that was

ultimately undesirable due to the potential light scattering properties, and cryo-EM was not performed with this ratio. The ratio of 1:4:72 resulted in a superfluous amount of nanodiscs without RyR1 incorporation and, as a consequence, cryo-EM studies were not performed with this ratio.

3.3.3. RyR2 Nanodisc Confirmation

The ratio of 1:2:36 was additionally tested on RyR2. The micrograph below depicts a section of one of the obtained micrographs (Figure 18).

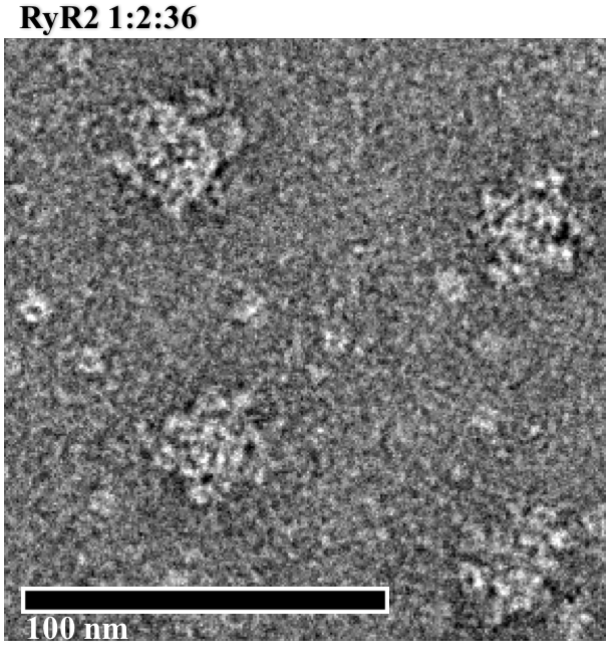

Figure 18. Confirmation of RyR2 insertion into nanodiscs

The molecules of RyR2 appear to retain their structural integrity as indicated by their standard square shape with an ‘X’ in the middle. This serves as a preliminary validation of successful insertion of the RyR2 into nanodiscs as all detergent was dialyzed from the sample in a previous

step. Since the nanodisc remains without detergent, it must be stabilizing the transmembrane region of the RyR2 leading to retention of structural integrity.

3.3.4. Visualization of the Nanodisc in RyR2

While investigating if the RyR2 could be incorporated into nanodiscs, one particular side view appeared to show the nanodisc in the transmembrane region the channel (Figure 19).

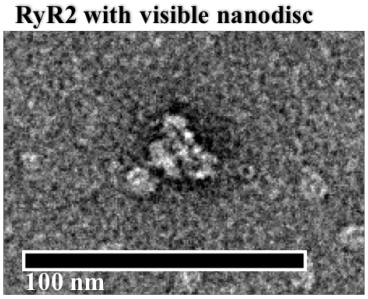

Figure 19. Negative stain side view seemingly depicting nanodisc insertion

In the above figure, there appears to be an extra density in the transmembrane region of the channel, and this is thought to be the first direct visualization of the nanodisc.

3.4. Cryo-EM using Tecnai F20 with a CCD Camera

3.4.1. Effects of low [NaCl]

For preliminary cryo-EM, a nanodisc ratio of 1:2:36 and a [NaCl] of 88 mM was used; the images below depict representative area of the obtained micrographs (Figure 20).

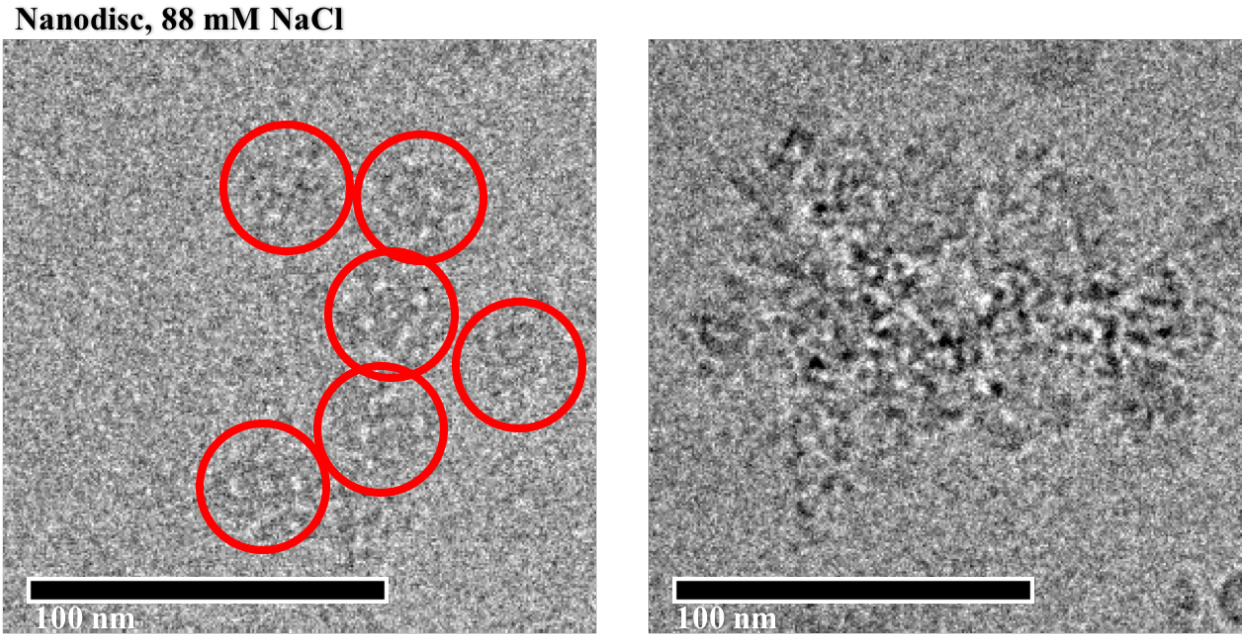

Figure 20. Cryo-EM of RyR1 at nanodisc ratio of 1:2:36 and [NaCl] of 88 mM

The particles are circled in red for easy recognition. As seen on the left, a portion of the RyR1 appear to be structurally intact and usable for single-particle analysis; however, the majority of them are not due to incorporation into aggregates. The image on the right depicts one of the many aggregates among this data set. Due to the very small amount of RyR1 present for single-particle analysis, the data was not analyzed by 2D or 3D classifications, and a new sample was attained with different parameters.

3.4.2. Observations of Increased [NaCl] and Tilted Images

Following the aggregation seen with a [NaCl] of 88 mM, the [NaCl] was increased to 500 mM, and a variety of properties including blotting time, blotting force, and blotting temperature were manipulated to alter the ice conditions from too thin and tearing to slightly thicker and more stable. Representative areas, one without stage tilt and one with 30º stage tilt, from micrographs of this data set are displayed below (Figure 21).

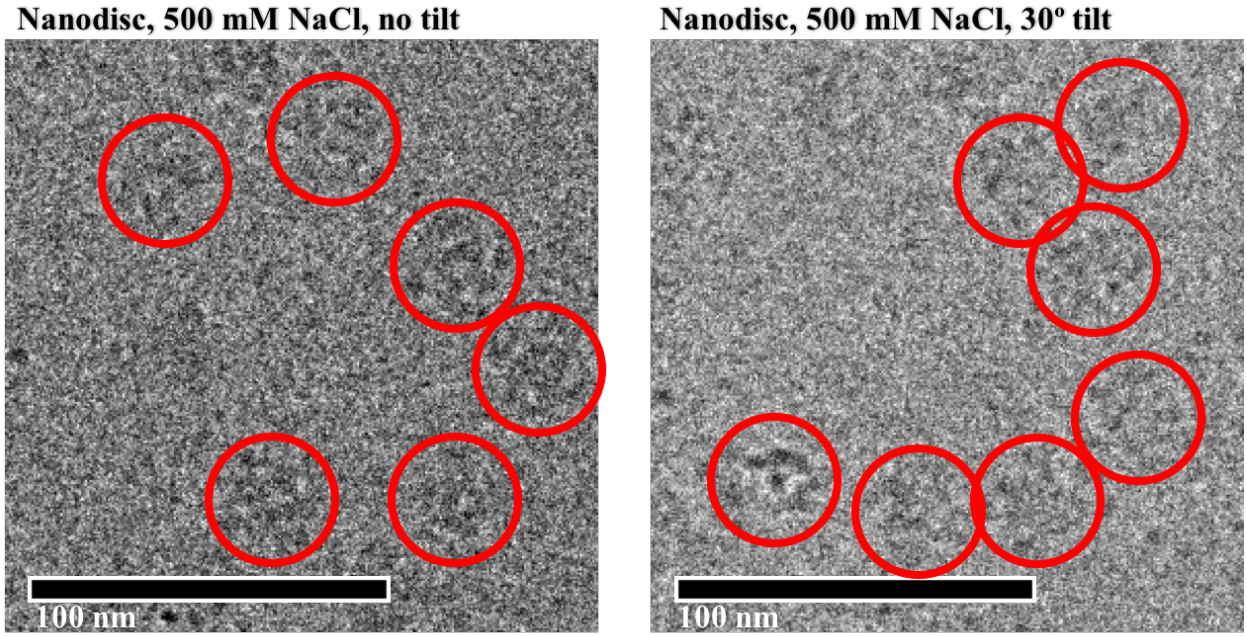

Figure 21. Comparison of cryo-EM of RyR1 at [NaCl] of 500 mM without stage tilt and with 30º stage tilt

The particles are circled in red for easy recognition. The initial data was collected without tilt and is depicted on the left; aggregates were present to a minimal extent, and the majority of the particles contained adequate space for picking like those seen above. The image on the right depicts the same grid preparation but with a stage tilt of 30º. The tilt orients the cytoplasmic

views in a configuration that exposes portions of the side of the RyR1 as means of trying to resolve more structure in those regions.

3.4.3. 2D Classification Using Relion without Tilted Images Incorporated

The micrographs without tilt were picked first using Boxer, and the coordinates were imported into Relion for 2D classification. Following 2D classification, the classes were analyzed, and the best were selected; the chosen classes for 3D classification are depicted below (Figure 22).

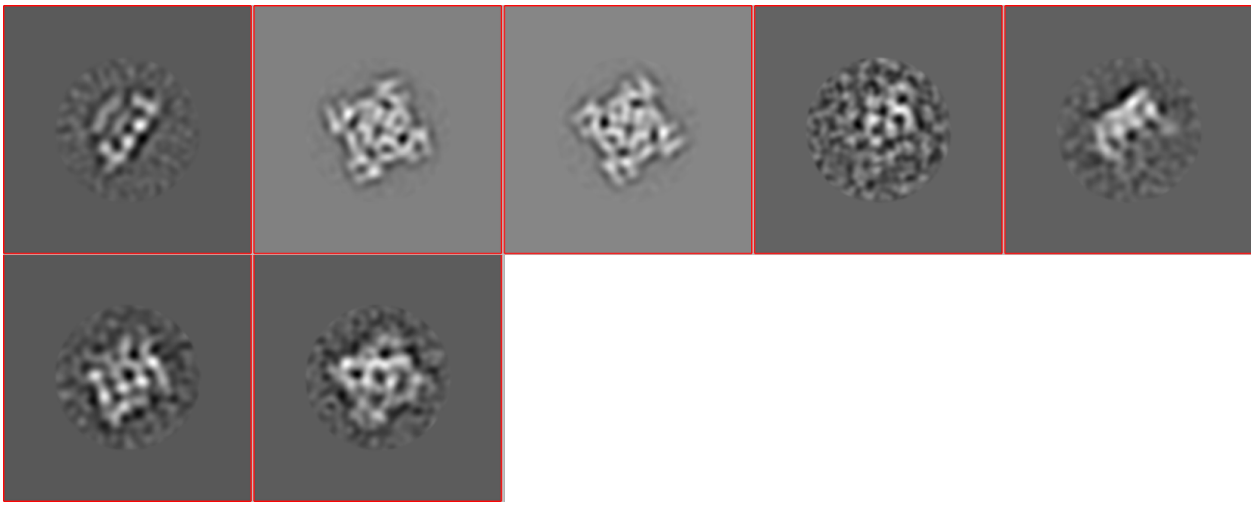

Figure 22. Classes of RyR1 without tilt

The majority of the views are of the cytoplasmic faces (2 and 3) of the RyR1 indicated by the low level of noise surrounding their 2D averages. The remaining five class averages have significant background noise but still show features of the RyR1; however, they comprise such a low percentage of the data set (less than 10%) that it was decided to collect more data with a stage tilt of 30º and 50º.

3.4.4. Spider and Frealign Classifications with Tilted Images Incorporated

Following acquisition of the tilted data, additional particles were picked and CTF parameters were determined using a CTF tilt software. These figures were sent for reference-based 2D classification using the Spider software, and the class averages are shown below (Figure 23).

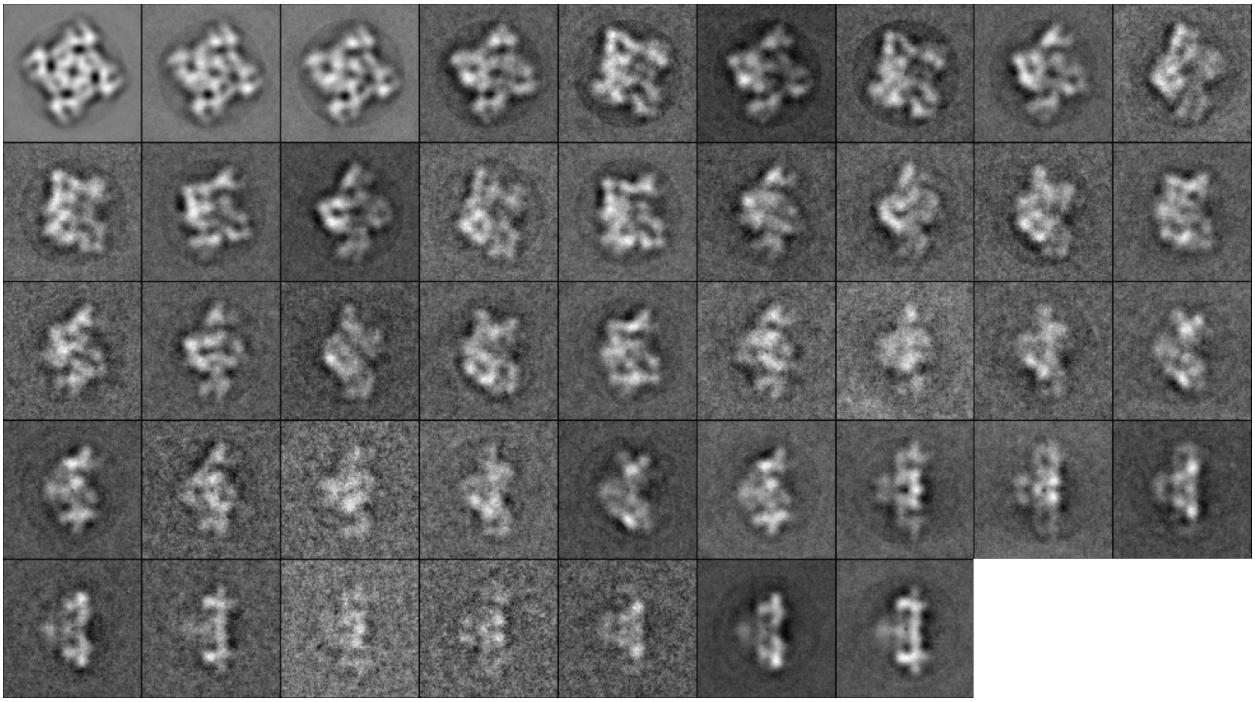

Figure 23. 2D class averages of RyR1 with incorporated tilted images using Spider

Analysis of the 2D class averages showed that approximately 9% of the images fell into the last two class averages (side views, bottom right). Additionally, the first 3 class averages (four-fold/top views, top left) only comprised about 37.5% of the data set indicating that the distribution is relatively well spread between each of the classes. As a consequence, the decision was made to send the data to Frealign for 3D refinement without limiting the amount of top views. The results of the 3D refinement are displayed below (Figure 24).

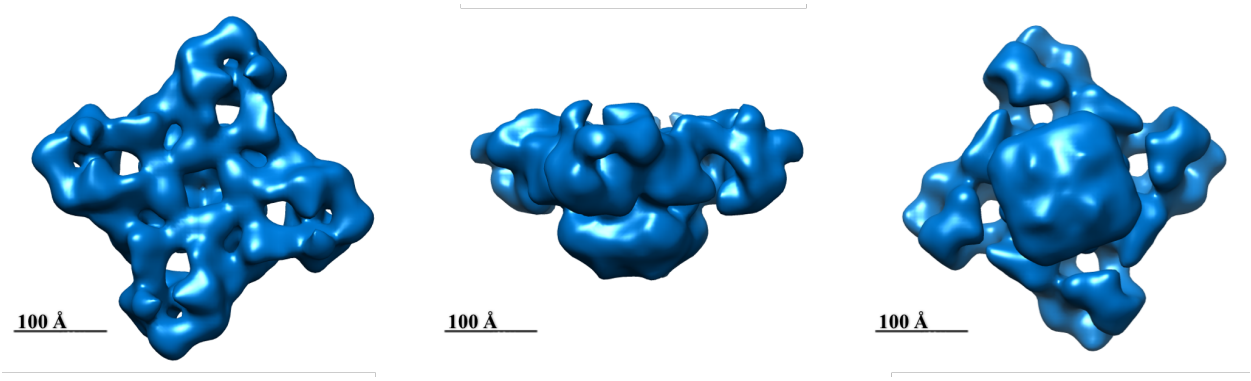

Figure 24. 3D density map of RyR1 with Mg^{2+} and AMP-PCP with tilted images incorporated

The overall resolution achieved was 20.97 Å based on the criteria of a 0.500 value on the Fourier Shell Correlation (FSC) curve. The presumed limiting factors of reaching the Nyquist limit of 9.32Å is the resulting noise from the thickness of vitreous ice and from the use of a CCD camera rather than a direct electron detector (DED).

3.5. Cryo-EM using Titan Krios with a DED

3.5.1. Image Acquisition and Microscope Settings

Using a K2 Summit direct electron detector in super resolution mode with a physical pixel size of 5 µm, 2083 micrographs were initially obtained. Table 1 describes the microscope settings used to acquire images.

Table 1. Microscope state for data collection using a direct electron detector		
Magnification: 105,000	Image Pixel Size: 0.66 Å	Nominal Dose: 41 e-/Å2
Spot Size: 9	Illuminated Area: 1.11 µm	Exposure Time: 12 sec
Binning: 1	Number of Frames: 40	Settling Time: 15 sec
Defocus Range: -1 to -2 µm	Defocus Step: 0.25 µm	Focus Interval: 6 µm

Following image acquisition, the images were gain corrected and low-pass filtered to 10 Å for particle picking. An example of a region of an acquired image is depicted below (Figure 25).

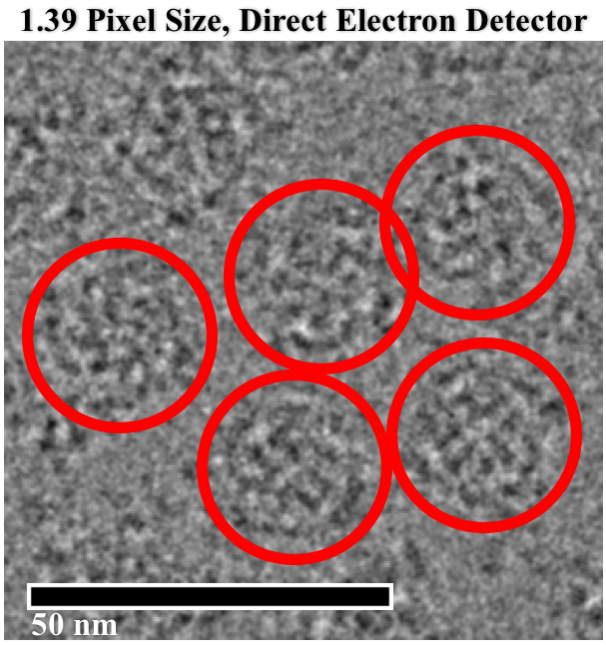

Figure 25. Sample region of micrograph collected with direct electron detector and low-pass filtered to 10Å

The red circles encapsulate particles from a sample region of the micrograph. As compared to the previous data collected with a CCD camera, the particles contain significantly more substructure despite filtering to 10 Å.

3.5.2. 2D and 3D Classification using Relion

Following particle picking on the first 1000 micrographs, autopicking was performed on the remaining 1083 micrographs, and the autopicked particles were screened for validity, while the false positives were removed. All 140,220 of the selected particles were imported into Relion for 2D classification in an effort to fully remove the non-particles for 3D classification; below is the selected classes from 2D classification that were ultimately sent for 3D classification (Figure 26).

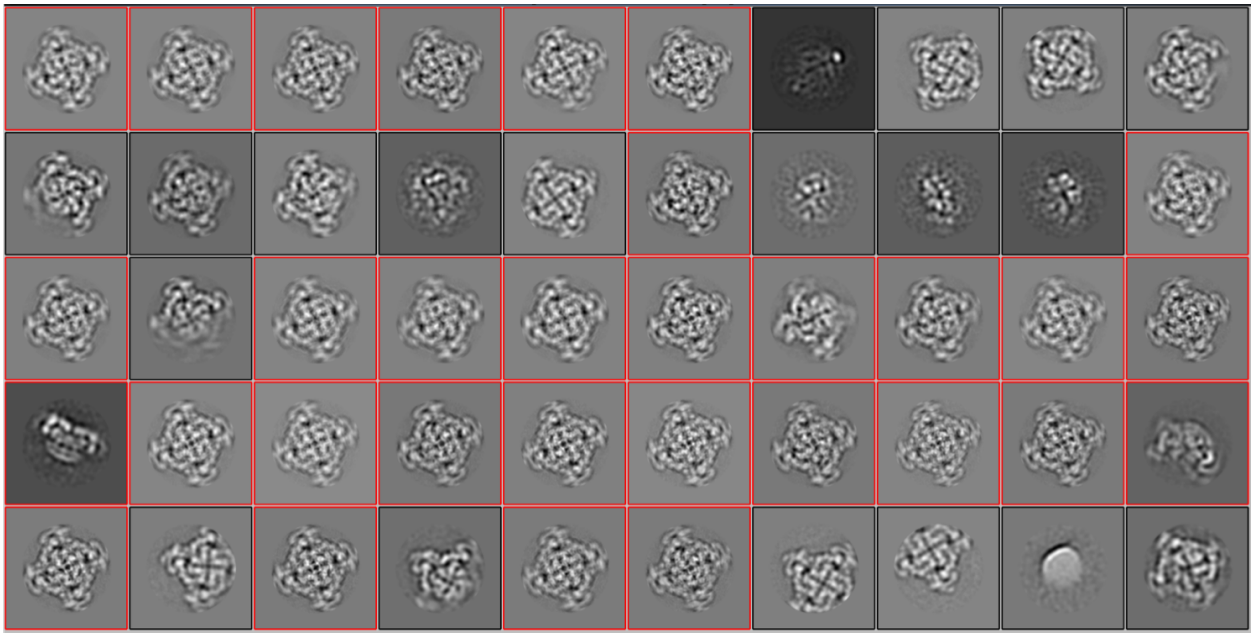

Figure 26. Selected classes from DED micrographs for 3D classification

The majority of the particles fell into the cytoplasmic (face) view category, and the software began classifying various cytoplasmic views based on defoci. There are 3 instances of non-cytoplasmic views in row three, column 10; row 4, column 1; and row 4, column 10. Despite the excess majority of views corresponding to cytoplasmic views, 3D classification was still performed on the data set; the 3D structure resulting from classification using Relion is depicted below (Figure 27).

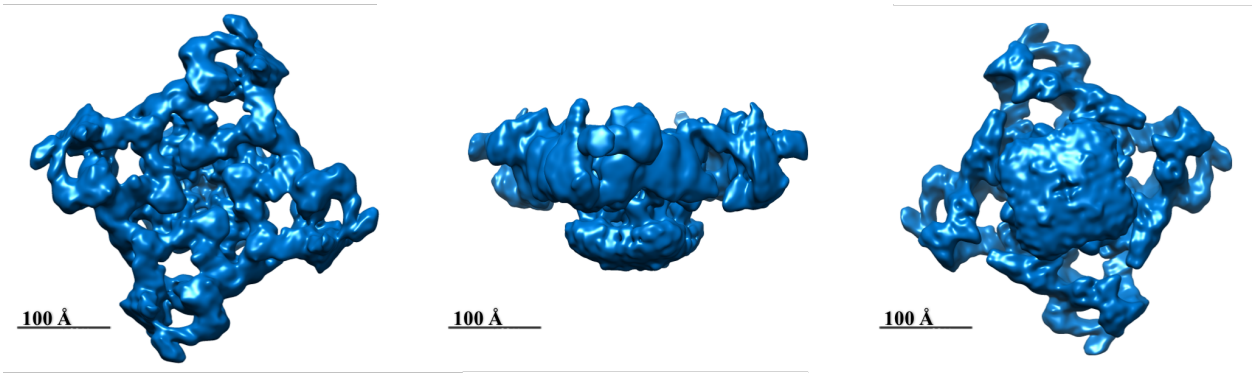

Figure 27. 3D density map of RyR1 with Mg^{2+} and AMP-PCP using 3D classification function of Relion

The overall resolution achieved from this 3D classification was 9.06 Å based on the criteria of a 0.500 value on the Fourier Shell Correlation (FSC) curve. Of note, the transmembrane helices do not appear to protrude below the lipid density at the luminal end of the receptor, so this lead to the decision to use another software for 3D reconstruction.

3.5.3. 2D Classification using Spider

Prior to 3D analysis, the 140,200 selected particles were re-screened to ensure that no particles were selected on the edge of the micrograph and that all the particles would be compatible with Frealign. This resulted in 136,586 particles being submitted for 2D classification and class averaging; the resulting averages are shown below (Figure 28).

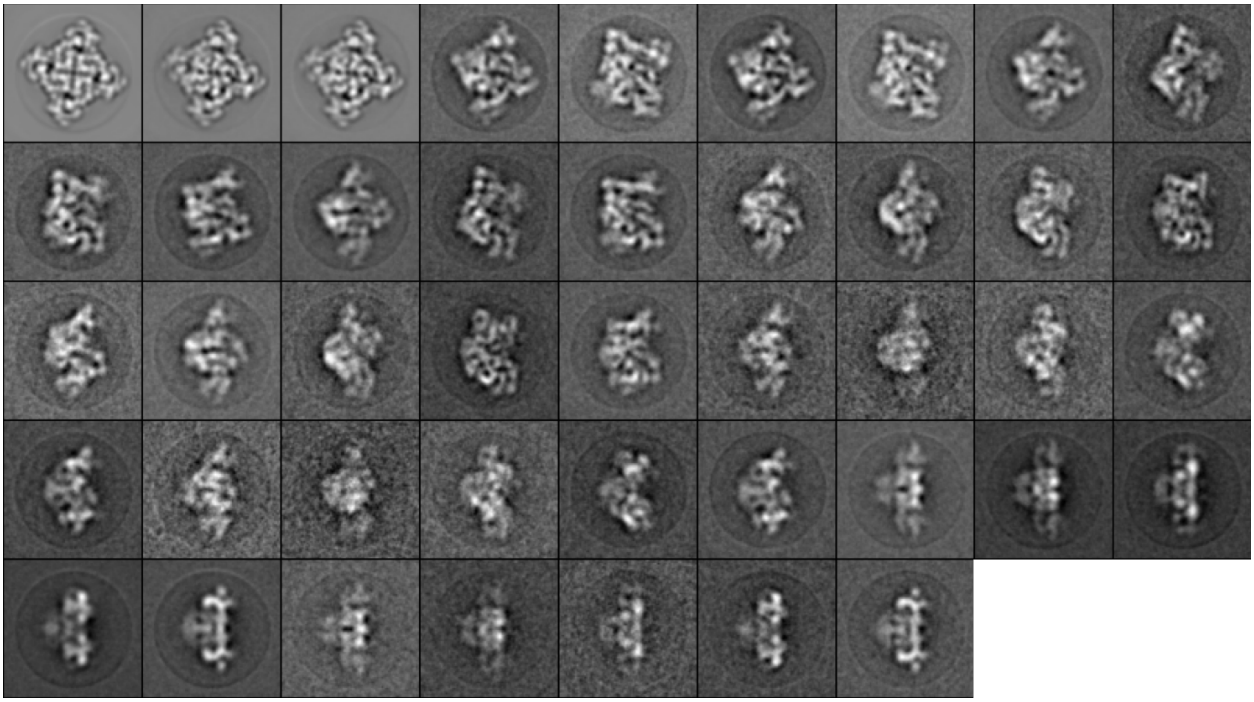

Figure 28. 2D class averages from DED micrographs formed using Spider

Analyzing the data, only 0.8% of the particles fell into the last two categories (side views, bottom right); that corresponds to 1,022 particles, which is even less than the number in the tilted

particle data set (1,672). Furthermore, 83,209, or approximately 61% of the data set, fell in the first class alone. As a consequence, it was deemed necessary to acquire more data using tilting of 40º in hopes of acquiring more side views and populating the other 42 classes in Figure 28.

3.5.4. 3D Classification using Frealign

Despite only having 1,022 side views, it was decided to proceed with processing the data in Frealign in hopes that the structural determination will perform better than Relion. The first class consisting of 83,209 particles was decreased in size to avoid any generation of artifact. The particles in this class were sorted in five categories of defoci, and approximately 3,000 particles from the first four defocus categories (0 µm to 2.5 µm) were selected and approximately 14,000 from the final defocus category (2.5 µm to 3.3 µm) for a total of 26,000 particles. The following figure depicts the distribution of particles into different orientation groups before and after removal of the excess (Figure 29).

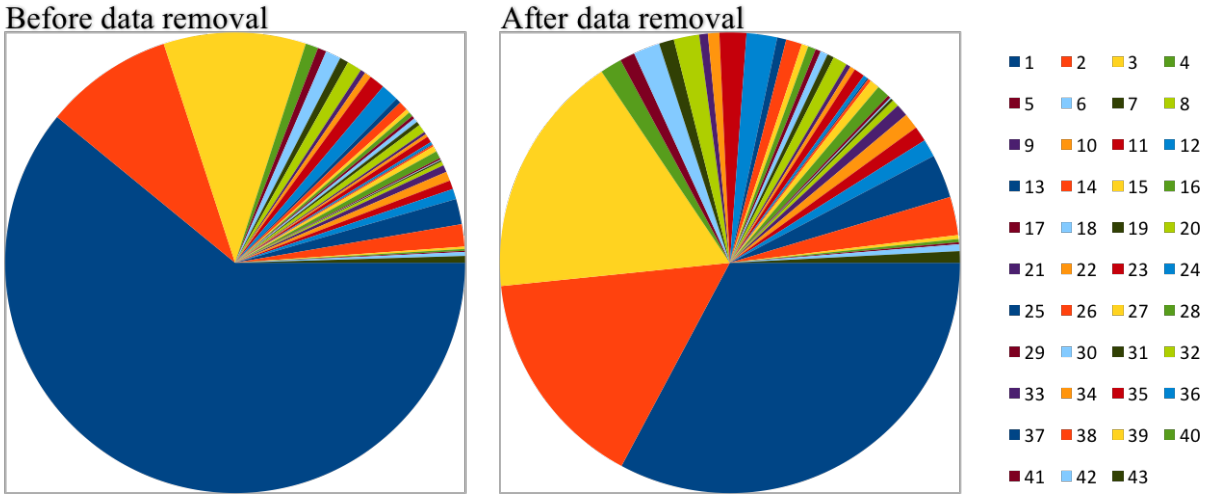

Figure 29. Distribution of particles in classes before and after data removal

The resulting data set consisting of 79,457 particles was sent to Frealign for 3D classification with only one 3D class and subsequent 3D refinement; the result of the refinement is depicted below (Figure 30).

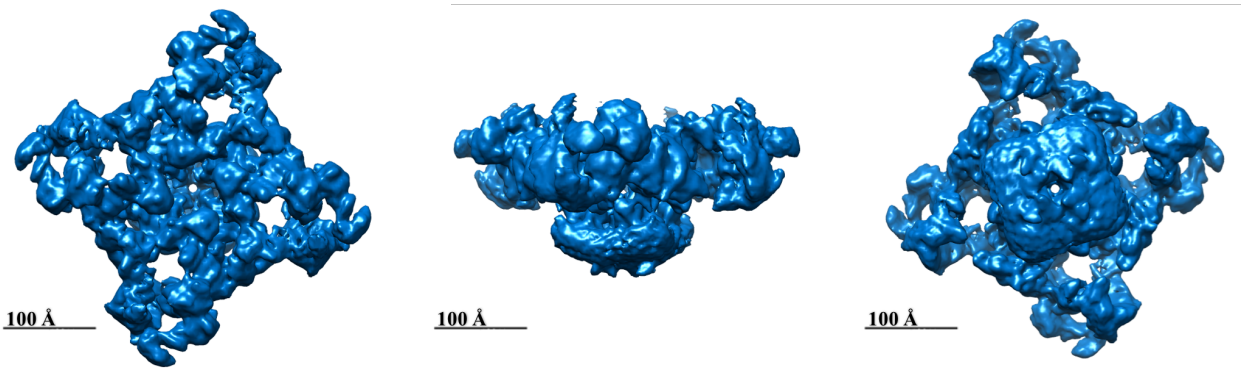

Figure 30. 3D density map of RyR1 with Mg^{2+} and AMP-PCP using 3D classification function of Frealign

Despite only achieving a resolution of 9.06 Å (identical to that of Relion) based on the criteria of a 0.500 value on the Fourier Shell Correlation (FSC) curve, the structure appears to be better for a number of reasons. First, the transmembrane helices appear to protrude below the lipid density at the luminal end of the receptor, unlike the structure from Relion. Additionally, the pore transcending the length of the receptor has been resolved; of note, this does not speak to the open or closed state of the receptor, and this will be addressed in later parts of the results and discussion. Lastly, all three faces of the RyR1, the cytoplasmic, side, and luminal faces, have more detail resolved than that of the Relion reconstruction. Consequently, this structure was used for the preliminary 3D analysis shown here until acquisition of tilted data is acquired and processing is performed.

3.5.5. Depiction of α-helices of RyR1

As a crude validation of a resolution of 9.06 Å, one may look for α-helices as they are only visible at resolutions under 10 Å. The figure below provides a view in which one may see α-helices (Figure 31).

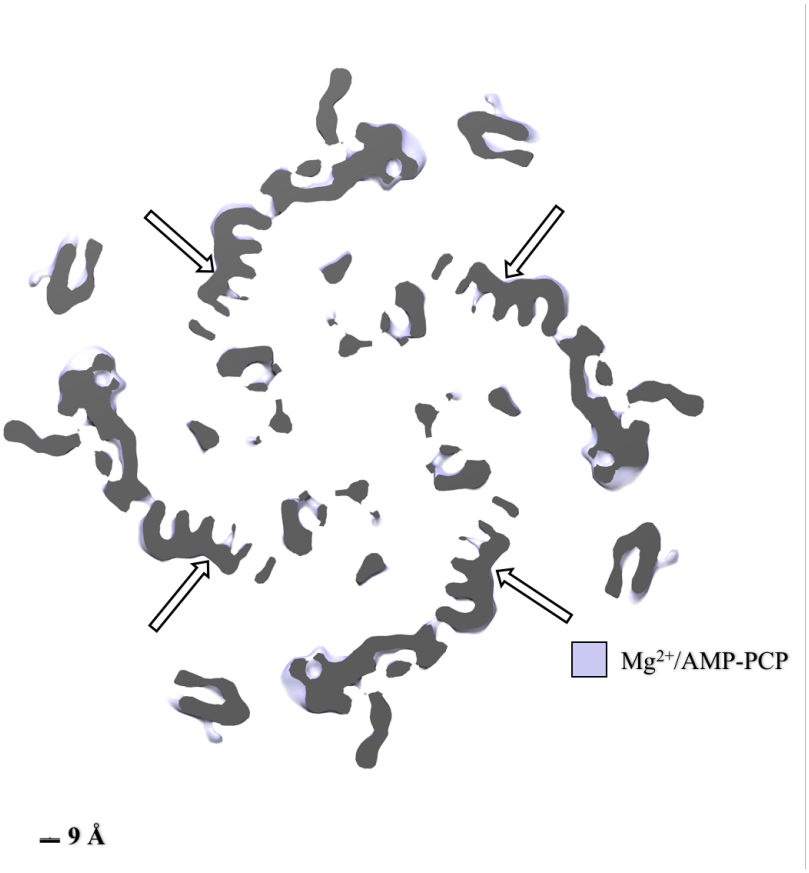

Figure 31. Depiction of α-helices in the 3D density map of RyR1 with Mg^{2+} and AMP-PCP

At the points of each of the four white arrows, the same comb-like pattern of α-helices from each of the four subunits are visible; these helices serve as validation that the states resolution is at least below 10 Å.

3.5.6. Analysis of FKBP12

As speculated, FKBP12 was removed during the sucrose gradient separation (Figure 32).

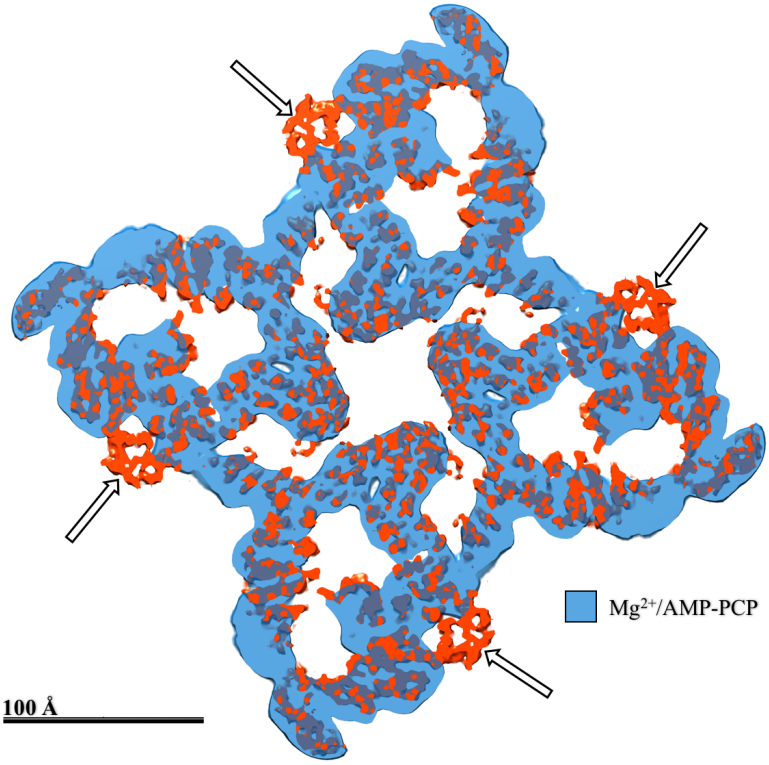

Figure 32. Depiction of lack of FKBP12 in the 3D density map of RyR1 with Mg^{2+} and AMP-PCP

The white arrows indicate the location of FKBP12 on the near-atomic resolution density map in red; this corresponds to the PDB ID of 3J8H and will be referenced to as such.[21] The density corresponding to FKBP12 does not appear on the density map of RyR1 with Mg^{2+} and AMP-PCP indicating that it was, in fact, removed during purification during the discontinuous sucrose gradient.

3.5.7. Depiction of Nanodisc in 3D Reconstruction.

As part of the initial negative staining studies, the goal was to optimize the ratio of RyR1:MSP:POPC for insertion into nanodiscs. Successful incorporation into nanodiscs was based on the assumption that the RyR1 was unstable without detergent and that, since detergent

was not present, the RyR1 had to be inserted into the nanodisc in order to retain its quaternary structure. Following 3D reconstruction, the transmembrane region may more clearly be visualized than 2D class averaging and, thus, assessed for the presence of a nanodisc. The following image shows the 3D reconstruction with Mg^{2+} and AMP-PCP as compared to the closed state of the RyR1 at 3.8 Å, 3J8H (Figure 33).[21]

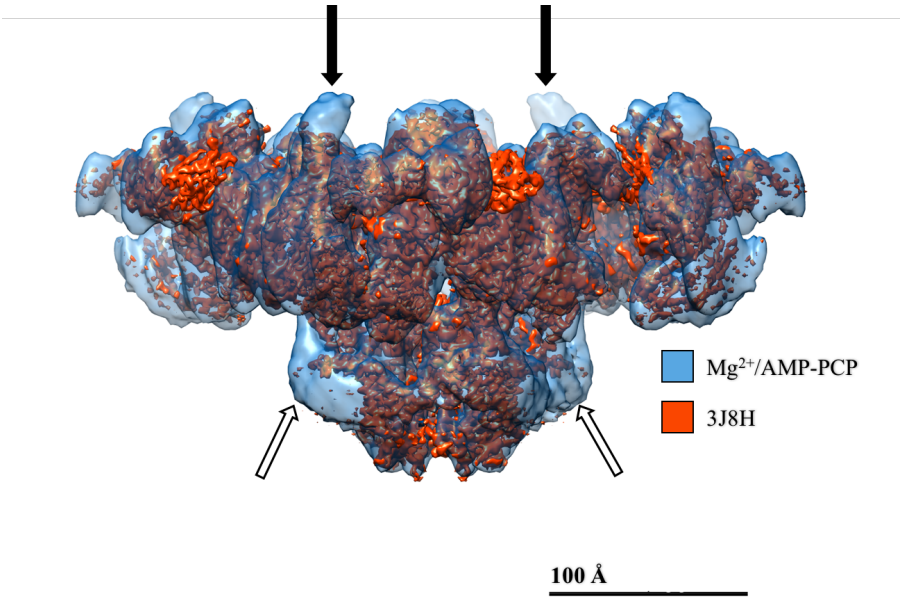

Figure 33. Depiction of the nanodisc from the side view in the 3D density map of RyR1 with Mg^{2+} and AMP-PCP

Firstly, the black arrows of Figure 33 depict the P2 domains of the RyR1 and how they protrude significantly more from the closed, near-atomic map of 3J8H. The P2 domain is typically a very unstable domain due to its flexibility, so this protrusion of the domain indicates that it has been stabilized, possible as a result of the addition of Mg^{2+} and AMP-PCP.

The extra density of blue indicated by the white arrows surrounding the red density of 3J8H corresponds to the nanodisc. This serves as validation that the RyR1 was, in fact, inserted into a nanodisc. It is possible to question why the nanodisc is unable to be visualized through negative

stain, and to answer this, one must analyze the nanodisc from the luminal view. The following figure shows the nanodisc from the luminal view of the RyR1 (Figure 34).

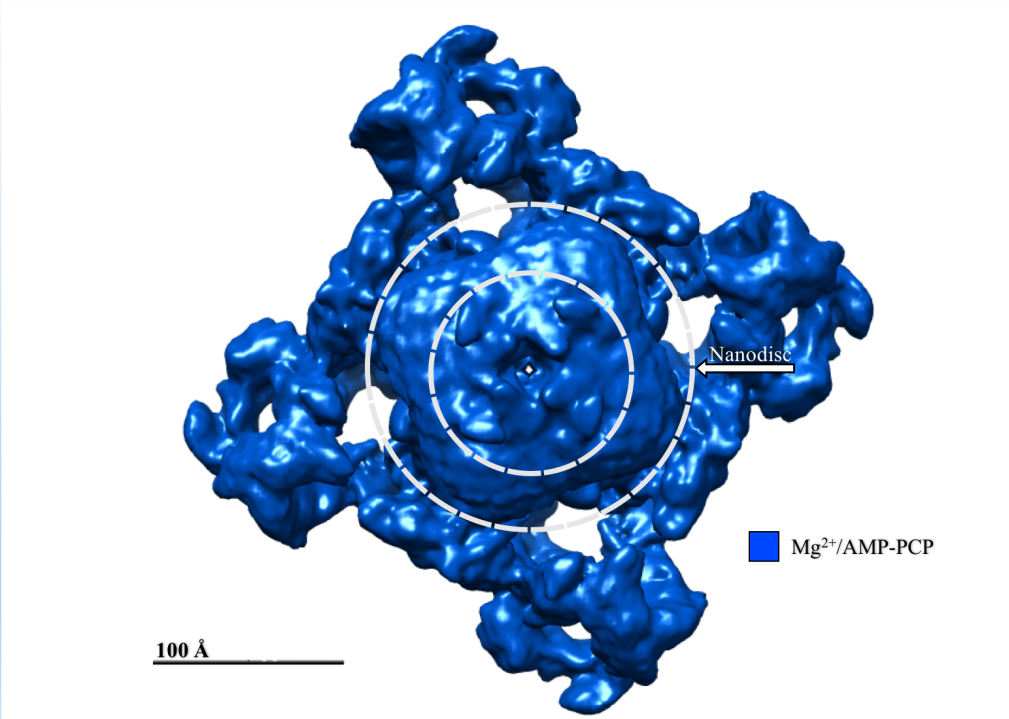

Figure 34. Depiction of the nanodisc from the luminal view in the 3D density map of RyR1 with Mg^{2+} and AMP-PCP

As indicated by the white arrows, even the most distal regions of the nanodisc are masked by the cytosolic face of the RyR1; as a consequence, one is unable to see the nanodisc from the cytoplasmic view. From the perspective of the luminal view, the nanodisc appears to blend with the under portion of the cytoplasmic face. Ultimately, the only view in which the nanodisc may be reliably visualized is the side view, and this, unfortunately, is the least common of the views. As a result, negative stain serves as a poor visual indicator of nanodisc insertion while 3D analysis provides more reliable confirmation.

3.5.8. Comparison to Open and Closed States

As part of the preliminary analysis, the RyR1 with Mg^{2+} and AMP-PCP was compared to the closed and open structures determined by Samsó et al. (2009); the figures below show those comparisons (Figure 35, 36, 37).[26]

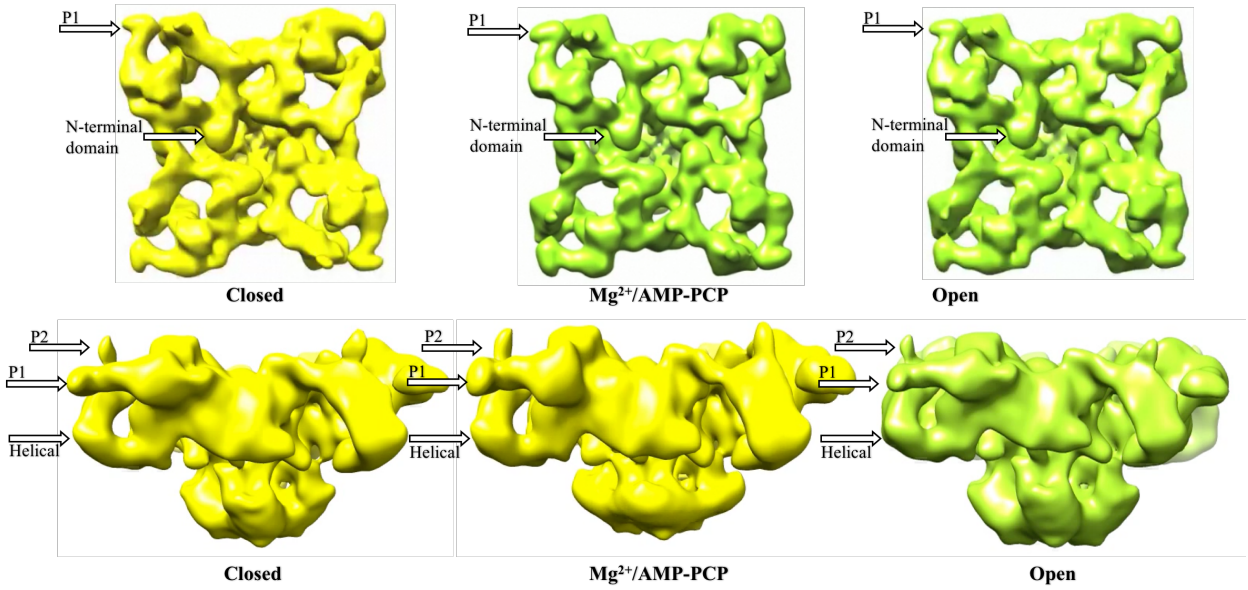

Figure 35. Overall comparison of cytoplasmic (top) and side views from 3D density map of RyR1 with Mg^{2+} and AMP-PCP to open and closed states of RyR1 from Samsó et al. (2009)[26]

Although difficult to analyze from the static images (more clear on a movie comparison), the RyR1 appears to be in an intermediate conformation between the open and closeds states. In the case of the transmembrane region at the site of the ion pore/gate, the RyR1 with Mg^{2+} and AMP-PCP reflects more the configuration of the closed channel; that is, the pore region is more closed than that of the open state.

The cytoplasmic region of the RyR1 reflects more the open state in two ways. Firstly, the N-terminal domains are more separated from one another, reflecting more the open conformation. And secondly, the helical domains seem to twist more forward in the comparison to the closed structure indicating that RyR1 with Mg^{2+} and AMP-PCP is in a state that is more similar to the open conformation.

Lastly, three features of the RyR1 appear unique and possibly the result of the addition of Mg^{2+} and AMP-PCP. Firstly, the P2 domains appear to move towards the SPRY3 domain. Secondly, the P1 domain appears wider than in both the closed and open conformations. And lastly, the EF hand motif on the underside of the cytoplasmic face of the RyR1 appears to enlarge, to move towards the transmembrane region of the receptor, and to connect with the S2/S3 extension of the transmembrane region.

The following figures, Figures 36 and 37, depict the ion gate as compared to the open and closed conformations of RyR1 from Samsó et al. (2009) to assess if the channel at the ion gate is in an open or closed configuration.[26]

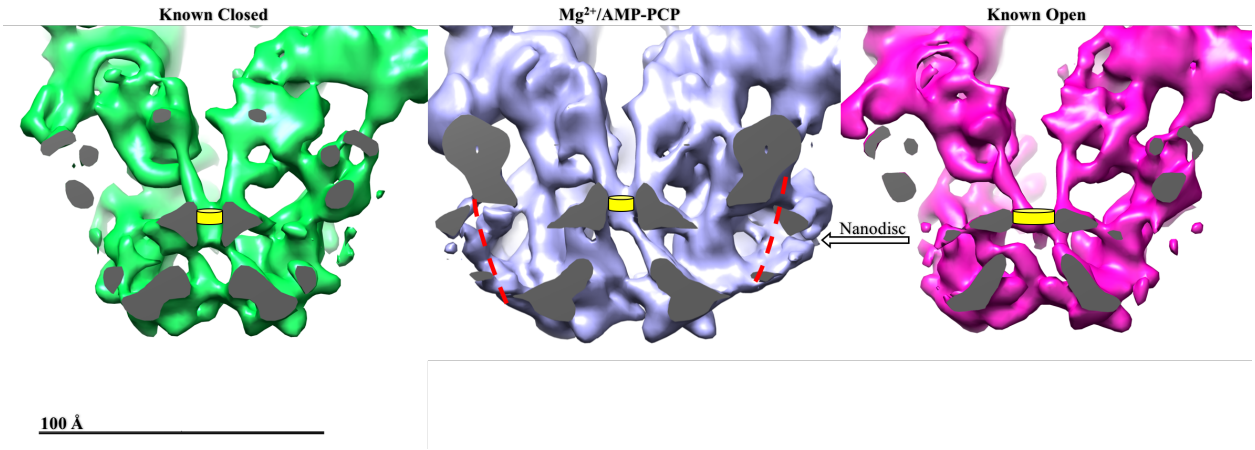

Figure 36. Side view comparison of the ion gate (yellow cylinder) from the 3D density map of RyR1 with Mg^{2+} and AMP-PCP to open and closed states of RyR1 from Samsó et al. (2009)[26]

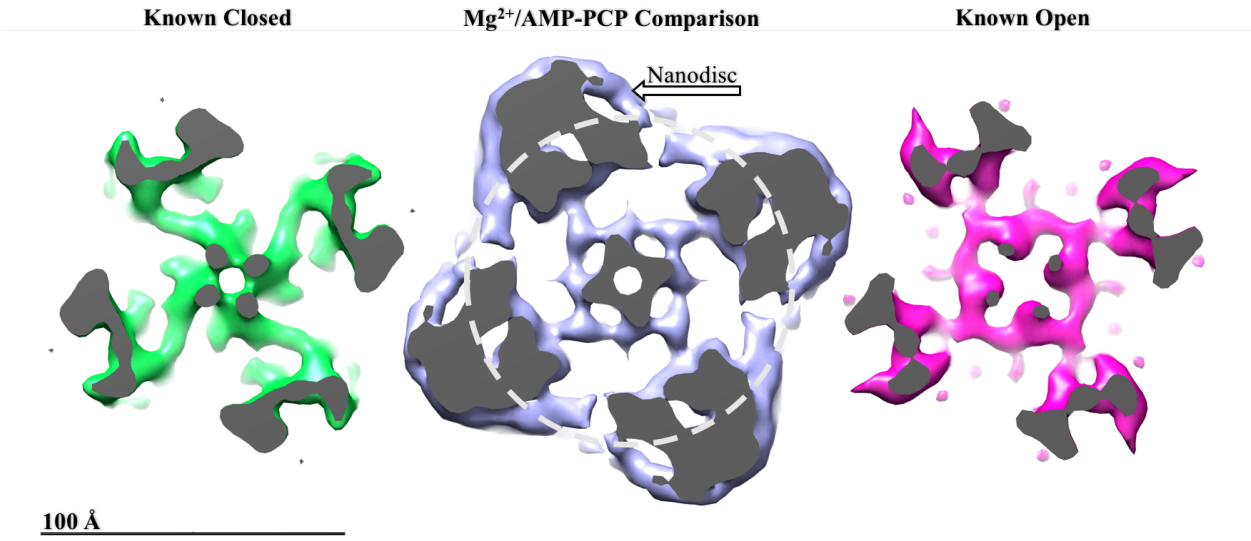

Figure 37. Cytoplasmic view comparison of the ion gate from the 3D density map of RyR1 with Mg^{2+} and AMP-PCP to open and closed states of RyR1 from Samsó et al (2009)[26]

As indicated by the yellow cylinders of Figure 36, the central region of the transmembrane region of the RyR1 corresponds to the ion gate, and it varies between the three density maps. Part of the differences may be accounted for differences in resolutions and data sets, but the channel shows other, clear differences. Relative to the first density map of the closed conformation, the ion gate width of RyR1 with Mg^{2+} and AMP-PCP appears similar. However, relative to the third density map of the open conformation, the ion gate width of RyR1 with Mg^{2+}/AMP-PCP is much more narrow.

This can be further visualized in Figure 37 using a section from the cytoplasmic (top) view of the RyR1 at the level of the ion gate. The first panel of Figure 37 depicts the closed conformation, the second depicts the density map of RyR1 with Mg^{2+} and AMP-PCP, and the third depicts the open conformation. The central blue densities corresponding to RyR1 with Mg^{2+} and AMP-PCP match well with the central green densities of the closed conformation, indicating that the two are in a similar conformation. The central blue densities of RyR1 with Mg^{2+} and AMP-PCP do

not match well with the central densities of the open conformation. As seen in the third panel, the pore size of the open conformation is significantly larger than the density map of RyR1 with Mg^{2+} and AMP-PCP indicating that the RyR1 is not in an open conformation. The minimum diameter of each of the pores was measured in Chimera (software), and the diameter of the ion gate in both the RyR1 with Mg^{2+} and AMP-PCP and the closed conformation was measured at approximately 8 Å. The minimum diameter of the open was determined at 12 Å, which is 4 Å larger than that of the RyR1 with Mg^{2+} and AMP-PCP. Despite this likely being sufficient to state that the conformation is closed, a second comparison with the RyR1 at near-atomic resolution was assessed to further validate these findings.[21]

3.5.9. Depiction of Ion Gate Compared to a Near-Atomic Map

As continued from the previous analysis, the ion gate structure was assessed once again to verify if the RyR1 is in the open configuration or closed configuration; the following slice of the 3D reconstruction depicts the ion gate as it is compared to the closed map of 3J8H (Figure 38).

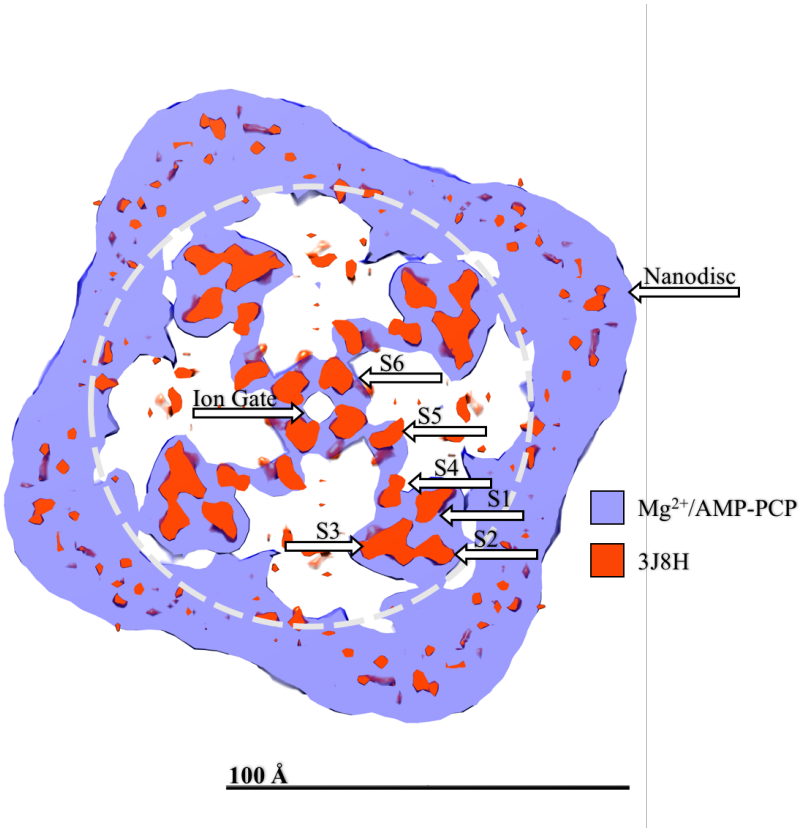

Figure 38. Depiction of the ion gate in the 3D density map of RyR1 with Mg^{2+} and AMP-PCP

As indicated by the white arrow, the ion gate is at the very center of the slice of RyR1. The lavender region corresponds to the density resolved by 3D refinement in Frealign, and the red region corresponds the closed map of 3J8H. At the site of the ion gate, the structure with Mg^{2+} and AMP-PCP has a comparable pore size similar to or possibly smaller than that of the closed state. Thus, it can be determined that this reconstruction is in a tightly closed state and that Mg^{2+} in the presence of AMP-PCP has an inhibiting effect.

As indicated by the white arrows, lavender densities of all 6 of the transmembrane helices are present within the transmembrane region, and there is a significant degree of overlap between the near-atomic closed configuration (3J8H) and the reconstruction with Mg^{2+} and AMP-PCP. This

degree of overlap serves as partial validation that the overall structure of the transmembrane region has been correctly resolved with Frealign.

4. Discussion

4.1. Protein Purification

The protein purification protocol was adapted from previous protocols used in our laboratory; the initial protocol did not require the addition of PC during the solubilization or sucrose gradient separation, but the lack of PC resulted in denaturation of the RyR1. Following incorporation of the PC to the protocol, no issues followed with regards to denaturation. Successful separation during the sucrose gradients depended immensely on meticulous attention to detail to keep the sucrose layers from mixing. The optimal protocol was to create the sucrose gradients as close to the ultracentrifuge as possible in an effort to minimize the amount of movement following creation the sucrose gradients. Also, addition of the protein sample to the sucrose gradients must be done just as slowly as the sucrose layers as another effort to prevent mixing of different layers.

Following sucrose gradient centrifugation, it was speculated that FKBP12 would not be bound to the RyR1 due to the separation based on molecular weight. This was confirmed in both the 3D reconstructions and in the 2D class averaging. FKBP12 was not added due to unpublished work from our laboratory showing aggregation of RyR1 in the presence of FKBP12, Mg^{2+}, and AMP-PCP and showing no aggregation of RyR1 in the presence of Mg^{2+} and AMP-PCP.

4.2. Nanodisc Ratio Determination and Successful Incorporation

The preliminary determination of a theoretical ratio of RyR1:MSP:POPC served as a starting point for empirical testing. The ratio of 1:2:50 was chosen as it was close to the theoretical ratio of 1:2:46 with a slight excess of POPC to account for any error. A ratio of 1:2:36 was tested as it had proven successful in preliminary attempts by our laboratory, and the ratio of 1:4:72 was chosen as a comparative point corresponding to double the MSP and POPC in the 1:2:36 ratio. The ratio of 1:2:70 was chosen arbitrarily as empirical point significantly higher than the theoretical.

Successful incorporation of the RyR1 into the nanodisc was based on the assumption that the presence of no detergent leads to degradation and aggregation, and since the detergent was dialyzed out following nanodisc formation, the RyR1 retaining its structural integrity is a consequence of successful incorporation. The sample was negatively stained for a number of reasons that include assessment of overall quality of RyR1, quality of RyR1 following insertion into nanodisc, purity of RyR1, and readiness for cryo-EM grid preparation.

The receptor was assessed prior to and after incorporation into nanodiscs using a ratio of RyR1:MSP:POPC of 1:2:36, and it was deemed successful due to the confirmed structural integrity of the receptor with negative staining method. Of note, the nanodisc was later visualized as a result of 3D reconstruction. This ratio of 1:2:36 was compared on two different occasions to three different ratios. First, the ratios of 1:2:50 and 1:2:70 were assessed; both proved successful, but the ratio of 1:2:70 lead to formation of large pockets of lipids that were thought to potentially

alter the light scattering properties of the sample. The ratio of 1:2:36 was then compared to the ratio of 1:4:72, and it was determined that doubling the concentrations of MSP and POPC relative to RyR1 lead to a large increase in the number of free nanodiscs. The ratio of 1:2:70 was also compared to the ratio of 1:4:72, and it was determined that use of more MSP with similar amounts of POPC lead to minimization of the amount of free POPC accumulating as it became incorporated into nanodiscs.

The preliminary decision was to use the ratios 1:2:36 as it incorporated a large portion of the RyR1 and minimized the amount of free nanodiscs. Ultimately, the ratio of 1:2:50 was chosen as it still minimized the amount of free nanodiscs but theoretically incorporated more RyR1. The ratio of 1:4:72 was not chosen due to the superfluous number of free nanodiscs that would require an extra step of purification to eliminate the excess.

The study is limited due to not testing the effect of dialyzing out the detergent without nanodiscs present. At the testing stage, limited supplies of rabbit muscle and purified RyR1 prevented testing a condition that would theoretically result in complete denaturation and aggregation of the already limited RyR1 stock.

4.3. Optimization of Cryo-EM Grid Preparation

A variety of parameters were altered to create a grid with thin enough ice to provide high resolution but thick enough to allow for different views of the receptor. To achieve the result, the parameters were altered systematically to assess the changes. The first parameter tested was pre-saturation; a cryogenic grid was visualized at room temperature before and after pre-saturation with 3 μL of sample applied for 60 seconds. It was determined that the pre-saturation step increased the occupancy of non-specific binding sites on the carbon support of the cryogenic grid, which would ultimately lead to increased concentration of RyR1 after plunge-freezing. Of note, the blotting following pre-saturation was performed by hand rather than using a Vitrobot. This, consequently, lead to a large variability in the thickness of the ice while holding all the other parameters constant. Nonetheless, the pre-saturation proved invaluable, so all freezing proceeded using pre-saturation.

The second parameter altered was the current associated with the glow discharge. The current was changed from 15 mA for 20 seconds to 25 mA for 20 seconds, but the difference in current did not show significant difference. As a result, the value of 15 mA was chosen as it provided sufficient concentration of protein and hydrophilicity of the grid.

Next, [NaCl] was altered following a preliminary test using 88 mM NaCl. The initial sample preparation did not account for the additions of Mg^{2+}, AMP-PCP, and EGTA needed to achieve the final conditions, so the [NaCl] was lower than anticipated. It was noted that the RyR1 aggregated following these additions despite significantly less aggregation on preliminary

sample checking during negative stain. Increasing the [NaCl] has been shown to decrease the interaction between multiple RyR1 due to it limiting of potential ionic interactions.[88] Consequently, it was found that increasing the [NaCl] to 500 mM lead to significantly less aggregation, and this was the value used in the subsequent freezing.

Lastly, the different parameters of blot force, blot time, and chamber temperature were manipulated. The results of these parameters proved less consistent than the previous parameters tested, but some general trends were observed. Decreasing the blot force resulted in thicker ice, so the blot force was decreased from 25 to 0. Decreasing the blot time resulted in thicker ice, so the blot time was decreased from 2 seconds to 0.5 seconds. Lastly, decreasing the temperature of the sample loading chamber resulted in less humidity contamination during freezing, so the temperature was decreased from room temperature, 25ºC to 4ºC.

4.4. Software Comparison Between Spider, Frealign, and Relion

Spider and Relion both have 2D class averaging; however, they differ immensely in the method and the ultimate result. Spider uses a reference-based classification system that compares each particle to projections of a 3D structure and determines a cross-correlation value that is used as criteria for classification. This method provides for very nice figures and classes but falls short in separating the particles from the non-particles because the non-particles are still placed in classes. The cross-correlation value can be used to limit the number of non-particles incorporated, but finding the threshold where only non-particles are omitted is a cumbersome task.

Relion, on the other hand, uses a reference-free classification system that generates its own averages based on comparing the selected particles to themselves. This proves valuable in removing non-particles from the data set, but does not generate as many classes based on projections. As a consequence, it becomes difficult to limit the number of particles of a certain orientation as other orientations are grouped into classes that do not reflect the true orientation.

In the case of this particular data set, the 2D class averaging and classification done through Spider served more valuable since the majority of the data fell into the first 3 categories of cytoplasmic views, and with Spider, these classes were able to be capped at 15,000 particles to prevent any artifact from forming. Following the 2D classification, the new data set consisting of 79,457 particles was submitted to both Relion and Frealign.

Both structures resolved 3D reconstructions with a resolution of 9.06 Å; however, the structure resulting from Frealign seemed to have more features/details despite the equivalent resolution. It is likely that there is a common region between the two 3D reconstructions that is limiting the achieved resolution, but Frealign was able to resolve more detail. With the incorporation of tilted data, more visualizations of the side of the RyR1 will be attained and added to the data set, and the resolution is expected to improve from 9.06 Å. Additionally, the ion gate and its pore were visualized more clearly with Frealign, and the transmembrane helices extended past the nanodisc in a manner more consistent with previously published reconstructions. It is likely that these differences resulted from lack of side views rather than from issues within either software, but for the sake of analysis, Frealign was more helpful in the current circumstance.

The resolution trends of the 3D structures deposited in the EMDataBank has been analyzed based on the software package used to perform the 3D reconstruction. The following figure depicts this analysis (Figure 39).[83]

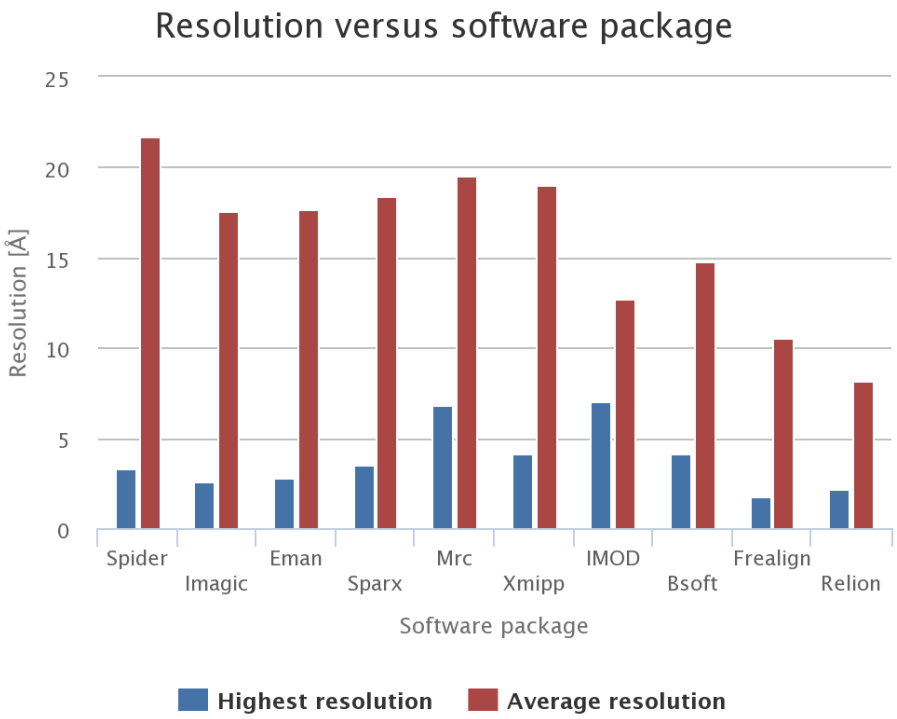

Figure 39. Graph of resolution trends based on software package of 3D structures deposited in EMDataBank adapted from Lawson et al. (2016)[83]

Based on the figure above, Spider does not typically serve as a good 3D reconstruction software as the average resolution of the 3D structures attained from the software is over 20 Å. Frealign and Relion are comparable in regards to both highest resolution achieved and average resolution. The highest resolution attained with Frealign is 1.8 Å, whereas the highest resolution attained with Relion is 2.2 Å. The average resolution attained with Frealign is 10.5 Å, whereas the average resolution attained with Relion is 8.1 Å. The differences in average resolution could possibly be explained by the increasing number of people beginning to use Relion in preference of Frealign. This result is in agreement with the results of the Relion and Frealign reconstruction of RyR1 with Mg^{2+} and AMP-PCP as they both returned identical resolutions. Nonetheless, in this particular incidence, Frealign proved slightly better for overall quality.

4.5. Conformation Effects of Mg^{2+} and AMP-PCP on the RyR1

Based on results from the 3D reconstruction using both Relion and Frealign, the nanodisc was resolved around the transmembrane region. This is, however, not the first successful incorporation of the RyR1 into nanodiscs; the following figure shows the first published data of RyR1 incorporated into a nanodisc (Figure 40).[89]

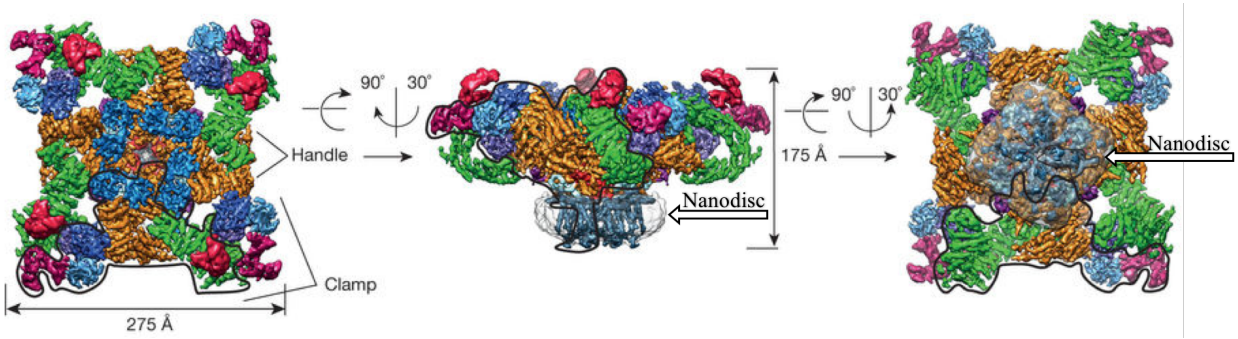

Figure 40. Cryo-EM density map depicting nanodisc adapted from Efremov et al. (2015)[89]

Although not the first incorporation, the optimization of the ratio of RyR1:MSP:POPC will undoubtedly prove valuable to our laboratory in this and future endeavors. It is worthy to note that the above diagram is currently the only published density map of RyR1 solubilized with nanodiscs. Since the density map of RyR1 with Mg^{2+} and AMP-PCP shows an identical shape and location of the nanodisc, the map depicting the nanodisc from Efremov is further validated.

The determination that RyR1 is closed in the presence of Mg^{2+} and AMP-PCP agrees with the expected result. The concentrations of Mg^{2+} and AMP-PCP used were in an effort to mimic the physiological state of the receptor, which is expected to be closed at rest given that the receptor

does not allow Ca^{2+} through the channel unless activated. However, the cytoplasmic region showed features of an open conformation.

In comparison to the structures of Samsó et al. (2009), the RyR1 with Mg^{2+} and AMP-PCP appeared to be in an intermediate conformation, "primed" to the open state for Ca^{2+} release. The cytoplasmic region of the RyR1 receptor reflected more the open conformation, whereas the transmembrane region and the ion gate of the receptor reflected more the closed conformation. Specifically, the N-terminal domain moved away from the pore region, and the helical domains did not twist towards the center of the receptor, both reflecting more of an open conformation. This opening effect may be the result of AMP-PCP having an activating/opening effect on the receptor. The closing of the ion gate/pore region may, conversely, be a result of the Mg^{2+} having an inhibitory effect, and the combined result leads to a primed channel with a closed ion gate and open conformation at the cytoplasmic portion.

In addition, some features were observed unique to the structure of RyR1 with Mg^{2+} and AMP-PCP. Those features (the stabilization and movement toward the SPRY3 domain of P2, the widening of P1, and the movement downward and connection to the S2/S3 extension) may be a result of the Mg^{2+}, the AMP-PCP, or the combination of the two. Further study is needed to assess if these differences are a consequence of Mg^{2+} and AMP-PCP or if they are a result of the presence of the nanodisc or the lack of FKBP12. This may be assessed by preliminary comparison to the previous structure with the nanodisc present and with closed structures containing FKBP12. Nonetheless, the true assessment will come from other testing of the RyR1 with only Mg^{2+}, only FKBP12, or only AMP-PCP present.

The biggest limitation of the structure is the resolution. Although an impressive 9.06 Å, the resolution is still not high enough to determine the sites of Mg^{2+} binding, which remains an

important aim of the study. With the upcoming incorporation of tilted data, the overall resolution will increase to a point where the molecules of Mg^{2+} will hopefully be able to be visualized.

Criticism may come with regards to not incorporating the FKBP12 or to using a higher [NaCl] than that of the physiological level. In regards to the FKBP12, unpublished aggregation lead to its lack of incorporation. In regards to the [NaCl], the level of [NaCl] higher than physiological levels was used as a means of preventing aggregation. Since Na^{+} has a minor activating effect and since the RyR1 resolved from 3D reconstruction is in a very inactive (closed) state, it can be inferred that Na^{+} did not significantly impact the conformation of the receptor

4.6. The Role of RyR1, Mg2+, and AMP-PCP in Malignant Hyperthermia

With the Böttcher et al. (1997), Hewat et al. (2007) and Bammes et al. (2017) results regarding the role of Mg^{2+} in malignant hyperthermia (MH) and in dantrolene treatment of MH, the importance of the result of this study has undeniably increased.[55,56,57] In the current state of the 3D reconstruction, determination that the receptor is in an inactive (closed) conformation validates that Mg^{2+} plays a vital role in regulating the RyR1 in physiological conditions. As a result, dysregulation of Mg^{2+} can be thought to lead to an open/leaky channel that is consistent with the phenotype of MH, and this further validates the current model that MH is Mg^{2+} dependent.

Following further 3D analysis and successful depiction of the Mg^{2+} binding site, a number of possibilities for further research will arise. Regulation studies regarding Mg^{2+} binding may be assessed, new binding sites may be identified, and areas for new drug therapy may be explored.

Subsequent analysis regarding Mg^{2+} may be performed with the aim of testing known mutations that lead to MH or CCD in an effort to assess if altering Mg^{2+} binding can lead to full closure of the receptor from a leaky conformation. Additionally, one may incorporate dantrolene into these experiments to further assess its conformational effects.

Bibliography

Bibliography

1 Hakamata Y, Nakai J, Takeshima H, Imoto K. Primary structure and distribution of a novel ryanodine receptor/calcium release channel from rabbit brain. FEBS Lett. 1992;312(2-3):229-35.

2 Pessah IN, Waterhouse AL, Casida JE. The calcium-ryanodine receptor complex of skeletal and cardiac muscle. Biochem Biophys Res Commun. 1985;128(1):449-56.

3 Fill M, Copello JA. Ryanodine receptor calcium release channels. Physiol Rev. 2002;82(4):893-922.

4 Eroschenko VP, Fiore MS. DiFiore's Atlas of Histology with Functional Correlations. Lippincott Williams & Wilkins; 2013.

5 Bernstein LH, Pearlman J, Lev-Ari A. The Centrality of Ca(2+) Signaling and Cytoskeleton Involving Calmodulin Kinases and Ryanodine Receptors in Cardiac Failure, Arterial Smooth Muscle, Post-ischemic Arrhythmia, Similarities and Differences, and Pharmaceutical Targets. LBPI Group. 2013.

6 Van Petegem F. Ryanodine receptors: allosteric ion channel giants. J Mol Biol. 2015;427(1):31-53.

7 Mccarthy TV, Quane KA, Lynch PJ. Ryanodine receptor mutations in malignant hyperthermia and central core disease. Hum Mutat. 2000;15(5):410-7.

8 Schneiderbanger D, Johannsen S, Roewer N, Schuster F. Management of malignant hyperthermia: diagnosis and treatment. Ther Clin Risk Manag. 2014;10:355-62.

9 Halliday NJ. Malignant hyperthermia. J Craniofac Surg. 2003;14(5):800-2.

10 Litman RS, Flood CD, Kaplan RF, Kim YL, Tobin JR. Postoperative malignant hyperthermia: an analysis of cases from the North American Malignant Hyperthermia Registry. Anesthesiology. 2008;109(5):825-9.

11 Rosenberg H, Pollock N, Schiemann A, Bulger T, Stowell K. Malignant hyperthermia: a review. Orphanet J Rare Dis. 2015;10:93.

12 Struk A, Lehmann-horn F, Melzer W. Voltage-dependent calcium release in human malignant hyperthermia muscle fibers. Biophys J. 1998;75(5):2402-10.

13 Baker KR, Landriscina D, Kartchner H, Mirkes DM. The Icarus effect: the influence of diluent warming on dantrolene sodium mixing time. AANA J. 2007;75(2):101-6.

14 Romero NB, Monnier N, Viollet L, et al. Dominant and recessive central core disease associated with RYR1 mutations and fetal akinesia. Brain. 2003;126(Pt 11):2341-9

15 Wallgren-Pettersson C. Commentationes Physico Mathematicae. University of Helsinki; 1990. Congenital nemaline myopathy: a longitudinal study.

16 Shuaib A, Paasuke RT, Brownell KW. Central core disease. Clinical features in 13 patients. Medicine (Baltimore). 1987;66(5):389-96.

17 Dubowitz V. Muscle disorders in childhood. 2nd. London , WB Saunders; 1995

18 Jungbluth H, Müller CR, Halliger-keller B, et al. Autosomal recessive inheritance of RYR1 mutations in a congenital myopathy with cores. Neurology. 2002;59(2):284-7.

19 Tong J, Mccarthy TV, Maclennan DH. Measurement of resting cytosolic Ca2+ concentrations and Ca2+ store size in HEK-293 cells transfected with malignant hyperthermia or central core disease mutant Ca2+ release channels. J Biol Chem. 1999;274(2):693-702.

20 Tung CC, Lobo PA, Kimlicka L, Van petegem F. The amino-terminal disease hotspot of ryanodine receptors forms a cytoplasmic vestibule. Nature. 2010;468(7323):585-8.

21 Yan Z, Bai XC, Yan C, et al. Structure of the rabbit ryanodine receptor RyR1 at near-atomic resolution. Nature. 2015;517(7532):50-5.

22 Yuchi Z, Yuen SM, Lau K, et al. Crystal structures of ryanodine receptor SPRY1 and tandem-repeat domains reveal a critical FKBP12 binding determinant. Nat Commun. 2015;6:7947.

23 Perálvarez-marín A, Tae H, Board PG, Casarotto MG, Dulhunty AF, Samsó M. 3D Mapping of the SPRY2 domain of ryanodine receptor 1 by single-particle cryo-EM. PLoS ONE. 2011;6(10):e25813.

24 Samsó M. A guide to the 3D structure of the ryanodine receptor type 1 by cryoEM. Protein Sci. 2017;26(1):52-68.

25 Chen Y, Xue S, Zou J, Lopez JR, Yang JJ, Perez CF. Myoplasmic resting Ca2+ regulation by ryanodine receptors is under the control of a novel Ca2+-binding region of the receptor. Biochem J. 2014;460(2):261-71.

26 Samsó M, Feng W, Pessah IN, Allen PD. Coordinated movement of cytoplasmic and transmembrane domains of RyR1 upon gating. PLoS Biol. 2009;7(4):e85.

27 Van Petegem F. How to open a Ryanodine Receptor. Cell Res. 2016;26(10):1073-1074.

28 Samsó M, Wagenknecht T, Allen PD. Internal structure and visualization of transmembrane domains of the RyR1 calcium release channel by cryo-EM. Nat Struct Mol Biol. 2005;12(6):539-44.

29 Meissner G, Darling E, Eveleth J. Kinetics of rapid Ca2+ release by sarcoplasmic reticulum. Effects of Ca2+, Mg2+, and adenine nucleotides. Biochemistry. 1986;25(1):236-44.

30 Smith JS, Coronado R, Meissner G. Single channel measurements of the calcium release channel from skeletal muscle sarcoplasmic reticulum. Activation by Ca2+ and ATP and modulation by Mg2+. J Gen Physiol. 1986;88(5):573-88.

31 Meissner G. Adenine nucleotide stimulation of Ca2+-induced Ca2+ release in sarcoplasmic reticulum. J Biol Chem. 1984;259(4):2365-74.

32 Dias JM, Vogel PD. Effects of small molecule modulators on ATP binding to skeletal ryanodine receptor. Protein J. 2009;28(5):240-6.

33 El-Ajouz S, Venturi E, Witschas K, et al. Dampened activity of ryanodine receptor channels in mutant skeletal muscle lacking TRIC-A. J Physiol (Lond). 2017;595(14): 4769–84

34 Copello JA, Barg S, Sonnleitner A, et al. Differential activation by Ca2+, ATP and caffeine of cardiac and skeletal muscle ryanodine receptors after block by Mg2+. J Membr Biol. 2002;187(1):51-64.

35 Chugun A, Sato O, Takeshima H, Ogawa Y. Mg2+ activates the ryanodine receptor type 2 (RyR2) at intermediate Ca2+ concentrations. Am J Physiol, Cell Physiol. 2007;292(1):C535-44.

36 Gomez AC, Yamaguchi N. Two regions of the ryanodine receptor calcium channel are involved in Ca(2+)-dependent inactivation. Biochemistry. 2014;53(8):1373-9.

37 Laver DR, Baynes TM, Dulhunty AF. Magnesium inhibition of ryanodine-receptor calcium channels: evidence for two independent mechanisms. J Membr Biol. 1997;156(3):213-29.

38 Smith JS, Coronado R, Meissner G. Single channel measurements of the calcium release channel from skeletal muscle sarcoplasmic reticulum. Activation by Ca2+ and ATP and modulation by Mg2+. J Gen Physiol. 1986;88(5):573-88.

39 Steele DS, Duke AM. Defective Mg2+ regulation of RyR1 as a causal factor in malignant hyperthermia. Arch Biochem Biophys. 2007;458(1):57-64.

40 Choi RH, Koenig X, Launikonis BS. Dantrolene requires Mg(2+) to arrest malignant hyperthermia. Proc Natl Acad Sci USA. 2017;114(18):4811-4815.

41 Fromm SA, Bharat TA, Jakobi AJ, Hagen WJ, Sachse C. Seeing tobacco mosaic virus through direct electron detectors. J Struct Biol. 2015;189(2):87-97.

42 Ahern GP, Junankar PR, Dulhunty AF. Subconductance states in single-channel activity of skeletal muscle ryanodine receptors after removal of FKBP12. Biophys J. 1997;72(1):146-62.

43 Tang W, Ingalls CP, Durham WJ, et al. Altered excitation-contraction coupling with skeletal muscle specific FKBP12 deficiency. FASEB J. 2004;18(13):1597-9.

44 Moore CP, Rodney G, Zhang JZ, Santacruz-toloza L, Strasburg G, Hamilton SL. Apocalmodulin and Ca2+ calmodulin bind to the same region on the skeletal muscle Ca2+ release channel. Biochemistry. 1999;38(26):8532-7.

45 Rodney GG, Williams BY, Strasburg GM, Beckingham K, Hamilton SL. Regulation of RYR1 activity by Ca(2+) and calmodulin. Biochemistry. 2000;39(26):7807-12.

46 Bayburt TH, Sligar SG. Membrane protein assembly into Nanodiscs. FEBS Lett. 2010;584(9):1721-7.

47 Shih AY, Freddolino PL, Arkhipov A, Schulten K. Assembly of lipoprotein particles revealed by coarse-grained molecular dynamics simulations. J Struct Biol. 2007;157(3):579-92.

48 Denisov IG, Grinkova YV, Lazarides AA, Sligar SG. Directed self-assembly of monodisperse phospholipid bilayer Nanodiscs with controlled size. J Am Chem Soc. 2004;126(11):3477-87.

49 Ritchie TK, Grinkova YV, Bayburt TH, et al. Chapter 11 - Reconstitution of membrane proteins in phospholipid bilayer nanodiscs. Meth Enzymol. 2009;464:211-31.

50 Denisov IG, Baas BJ, Grinkova YV, Sligar SG. Cooperativity in cytochrome P450 3A4: linkages in substrate binding, spin state, uncoupling, and product formation. J Biol Chem. 2007;282(10):7066-76.

51 Polayes DA, Parks TD, Johnston SA, Dougherty WG. Application of TEV Protease in Protein Production. Methods Mol Med. 1998;13:169-83.

52 Cabra V, Samsó M. Do's and don'ts of cryo-electron microscopy: a primer on sample preparation and high quality data collection for macromolecular 3D reconstruction. J Vis Exp. 2015;(95):52311.

53 Milne JL, Borgnia MJ, Bartesaghi A, et al. Cryo-electron microscopy--a primer for the non-microscopist. FEBS J. 2013;280(1):28-45.

54 Pelletier J, Pomot C. Work function of sintered lanthanum hexaboride. Applied Physics Letters, 1979;34(4):249-51.

55 Böttcher B, Wynne SA, Crowther RA. Determination of the fold of the core protein of hepatitis B virus by electron cryomicroscopy. Nature. 1997;386(6620):88-91.

56 Hewat EA, Neumann E. Characterization of the performance of a 200-kV field emission gun for cryo-electron microscopy of biological molecules. J Struct Biol. 2002;139(1):60-4.

57 Bammes BE, Rochat RH, Jakana J, Chen DH, Chiu W. Direct electron detection yields cryo-EM reconstructions at resolutions beyond 3/4 Nyquist frequency. J Struct Biol. 2012;177(3):589-601.

58 Bammes BE, Rochat RH, Jakana J, Chiu W. Practical performance evaluation of a 10k × 10k CCD for electron cryo-microscopy. J Struct Biol. 2011;175(3):384-93.

59 Milazzo AC, Cheng A, Moeller A, et al. Initial evaluation of a direct detection device detector for single particle cryo-electron microscopy. J Struct Biol. 2011;176(3):404-8.

60 Turchetta R, Berst JD, Casadei B, et al. A monolithic active pixel sensor for charged particle tracking and imaging using standard VLSI CMOS technology. Nucl Instr Meth Phys Res. 2001;458(3):677-89.

61 Fromm SA, Bharat TA, Jakobi AJ, Hagen WJ, Sachse C. Seeing tobacco mosaic virus through direct electron detectors. J Struct Biol. 2015;189(2):87-97.

62 Karuppasamy M, Karimi nejadasl F, Vulovic M, Koster AJ, Ravelli RB. Radiation damage in single-particle cryo-electron microscopy: effects of dose and dose rate. J Synchrotron Radiat. 2011;18(Pt 3):398-412.

63 Burmeister WP. Structural changes in a cryo-cooled protein crystal owing to radiation damage. Acta Crystallogr D Biol Crystallogr. 2000;56(Pt 3):328-41.

64 Rawson S, Iadanza MG, Ranson NA, Muench SP. Methods to account for movement and flexibility in cryo-EM data processing. Methods. 2016;100:35-41.

65 Bai XC, Fernandez IS, McMullan G, Scheres SH. Ribosome structures to near-atomic resolution from thirty thousand cryo-EM particles. Elife. 2013;2:e00461.

66 Zheng SQ, Palovcak E, Armache JP, Verba KA, Cheng Y, Agard DA. MotionCor2: anisotropic correction of beam-induced motion for improved cryo-electron microscopy. Nat Methods. 2017;14(4):331-332.

67 Zhang K. Gctf: Real-time CTF determination and correction. J Struct Biol. 2016;193(1):1-12.

68 Yang C, Jiang W, Chen DH, Adiga U, Ng EG, Chiu W. Estimating contrast transfer function and associated parameters by constrained non-linear optimization. J Microsc. 2009;233(3):391-403.

69 Cheng Y, Grigorieff N, Penczek PA, Walz T. A primer to single-particle cryo-electron microscopy. Cell. 2015;161(3):438-49.

70 Ranson N. Cryo-Electron Microscopy of Viruses In: Stockley PG, Twarock R, ed. Emerging Topics in Physical Virology. World Scientific; 2010: 1-33.

71 McMullan G, Faruqi AR, Clare D, Henderson R. Comparison of optimal performance at 300keV of three direct electron detectors for use in low dose electron microscopy. Ultramicroscopy. 2014;147:156-63.

72 Li X, Zheng SQ, Egami K, Agard DA, Cheng Y. Influence of electron dose rate on electron counting images recorded with the K2 camera. J Struct Biol. 2013;184(2):251-60.

73 Ludtke SJ, Baldwin PR, Chiu W. EMAN: semiautomated software for high-resolution single-particle reconstructions. J Struct Biol. 1999;128(1):82-97.

74 Scheres SH. Semi-automated selection of cryo-EM particles in RELION-1.3. J Struct Biol. 2015;189(2):114-22.

75 Penczek PA. Resolution measures in molecular electron microscopy. Meth Enzymol. 2010;482:73-100.

76 Rosenthal PB, Henderson R. Optimal determination of particle orientation, absolute hand, and contrast loss in single-particle electron cryomicroscopy. J Mol Biol. 2003;333(4):721-45.

77 Maurer SP, Fourniol FJ, Bohner G, Moores CA, Surrey T. EBs recognize a nucleotide-dependent structural cap at growing microtubule ends. Cell. 2012;149(2):371-82.

78 Shaikh TR, Gao H, Baxter WT, et al. SPIDER image processing for single-particle reconstruction of biological macromolecules from electron micrographs. Nat Protoc. 2008;3(12):1941-74.

79 Grigorieff N. FREALIGN: high-resolution refinement of single particle structures. J Struct Biol. 2007;157(1):117-25.

80 Henderson R. Avoiding the pitfalls of single particle cryo-electron microscopy: Einstein from noise. Proc Natl Acad Sci USA. 2013;110(45):18037-41.

81 Kaufmann KW, Lemmon GH, Deluca SL, Sheehan JH, Meiler J. Practically useful: what the Rosetta protein modeling suite can do for you. Biochemistry. 2010;49(14):2987-98.

82 Fernandez-Leiro R, Scheres SH. Unravelling biological macromolecules with cryo-electron microscopy. Nature. 2016;537(7620):339-46.

83 Lawson CL, Patwardhan A, Baker ML, et al. EMDataBank unified data resource for 3DEM. Nucleic Acids Res. 2016;44(D1):D396-403.

84 Cheng Y. Single-Particle Cryo-EM at Crystallographic Resolution. Cell. 2015;161(3):450-7.

85 Schoenmakers TJ, Visser GJ, Flik G, Theuvenet AP. CHELATOR: an improved method for computing metal ion concentrations in physiological solutions. BioTechniques. 1992;12(6):870-4, 876-9.

86 Balshaw DM, Xu L, Yamaguchi N, Pasek DA, Meissner G. Calmodulin binding and inhibition of cardiac muscle calcium release channel (ryanodine receptor). J Biol Chem. 2001;276(23):20144-53.

87 Blazev R, Lamb GD. Low [ATP] and elevated [Mg2+] reduce depolarization-induced Ca2+ release in rat skinned skeletal muscle fibres. J Physiol (Lond). 1999;520 Pt 1:203-15.

88 Dhindwal S, Lobo J, Cabra V, et al. A cryo-EM-based model of phosphorylation- and FKBP12.6-mediated allosterism of the cardiac ryanodine receptor. Sci Signal. 2017;10(480)

89 Efremov RG, Leitner A, Aebersold R, Raunser S. Architecture and conformational switch mechanism of the ryanodine receptor. Nature. 2015;517(7532):39-43.

Vita

Alex H. Will was born on July 7th, 1992, in Phalaborwa, South Africa. He moved to Richmond, Virginia in 1998. He received his Bachelor of Science in chemistry with a specialization in biochemistry from the University of Virginia in 2014. Alex worked at the University of Virginia Emergency Department from December of 2013 until July of 2015. He then returned to Richmond, Virginia to enter graduate school at Virginia Commonwealth University's Pre-Medical Graduate Health Sciences Certificate Program. Upon completion of the program in 2016, Alex joined Dr. Montserrat Samsó's laboratory to pursue a Master of Physiology and Biophysics. In June of 2017, he was accepted to medical school at Virginia Commonwealth University, where he will be attending starting in August of 2017. Alex's interests include emergency medicine, anesthesiology, cardiology, and orthopedics.